Antarctic Sea Ice Extent Variability and Its Global Connectivity*

XIAOJUN YUAN AND DOUGLAS G. MARTINSON

Lamont-Doherty Earth Observatory and Department of Earth and Environmental Sciences, Columbia University, Palisades, New York

(Manuscript received 18 July 1997, in final form 29 July 1999)

ABSTRACT

This study statistically evaluates the relationship between Antarctic sea ice extent and global climate variability. Temporal cross correlations between detrended Antarctic sea ice edge (SIE) anomaly and various climate indices are calculated. For the sea surface temperature (SST) in the eastern equatorial Pacific and tropical Indian Ocean, as well as the tropical Pacific precipitation, a coherent propagating pattern is clearly evident in all correlations with the spatially averaged (over 12° longitude) detrended SIE anomalies (⟨SIE*⟩). Correlations with ENSO indices imply that up to 34% of the variance in ⟨SIE*⟩ is linearly related to ENSO. The ⟨SIE*⟩ has even higher correlations with the tropical Pacific precipitation and SST in the tropical Indian Ocean. In addition, correlation of ⟨SIE*⟩ with global surface temperature produces four characteristic correlation patterns: 1) an ENSO-like pattern in the Tropics with strong correlations in the Indian Ocean and North America ($r > 0.6$); 2) a teleconnection pattern between the eastern Pacific region of the Antarctic and western–central tropical Pacific; 3) an Antarctic dipole across the Drake Passage; and 4) meridional banding structures in the central Pacific and Atlantic expending from polar regions to the Tropics, even to the Northern Hemisphere.

The SIE anomalies in the Amundsen Sea, Bellingshausen Sea, and Weddell Gyre of the Antarctic polar ocean sectors show the strongest polar links to extrapolar climate. Linear correlations between ⟨SIE*⟩ in those regions and global climate parameters pass a local significance test at the 95% confidence level. The field significance, designed to account for spatial coherence in the surface temperature, is evaluated using quasiperiodic colored noise that is more appropriate than white noise. The fraction of the globe displaying locally significant correlations (at the 95% confidence level) between ⟨SIE*⟩ and global temperature is significantly larger, at the 99.5% confidence level, than the fraction expected given quasiperiodic colored noise in place of the ⟨SIE*⟩. Based on EOF analysis and multiplicity theory, the four teleconnection patterns the authors found are the ones reflecting correlations most likely to be physically meaningful.

1. Introduction

The polar regions, through their sea ice cover, ice sheets, and deep-water formation–ventilation sites, have the potential to influence global climate over a broad range of timescales (e.g., Fletcher 1969; Walsh 1983). In fact, numerous modeling studies suggest such an influence through the sea ice fields alone. On short timescales, for example, Grumbine (1994) has shown that local winds influence lead area and albedo, whose effects are telecommunicated within a few days to midlatitudes. On longer timescales, Meehl and Washington (1990) obtained a warmer global mean climate and increased global-averaged sensitivity to doubled atmospheric CO_2 in an atmospheric general circulation model (GCM) when using an improved snow–ice albedo scheme. More recently, global climate simulations using the Goddard Institute for Space Studies (GISS) GCM (Hansen et al. 1983), under conditions of doubled atmospheric CO_2, showed that 37% of the annual average global warming in that model is attributed to the nonlinear feedbacks driven by changes in sea ice above and beyond the linear ice-albedo feedback (Rind et al. 1995). Other examples of the sea ice influences are given in the review of Meehl (1984) and, for example, in Meehl (1988, 1990) and Bromwich et al. (1998).

In addition to modeling studies, satellite observations, since the early 1970s, have provided an opportunity to study interannual variabilities of sea ice (e.g., Zwally et al. 1983; Gloersen et al. 1992; Parkinson 1992, 1994; Gloersen 1995; Stammerjohn and Smith 1996) and its covariation with global climate. A number of such studies have suggested that the Antarctic sea ice fields linearly covary with the tropical Pacific El Niño–Southern Oscillation (ENSO) phenomenon (e.g., Chiu 1983; Carleton 1989; Simmonds and Jacka 1995; Yuan et al. 1996; Ledley and Huang 1997). Gloersen (1995), using multiple-window harmonic analysis, found that sea ice

* Lamont-Doherty Earth Observatory Contribution Number 5973.

Corresponding author address: Dr. Xiaojun Yuan, Lamont-Doherty Earth Observatory, Columbia University, 61 RT 9W, Palisades, NY 10964-8000.
E-mail: xiaojun@ice.ldeo.columbia.edu

in both the Arctic and Antarctic contains quasi-biennial and quasi-quadrennial periodicities that are associated with ENSO variation. More recently, White and Peterson (1996) reported that anomalies in the Antarctic sea ice extent, as well as anomalies in sea surface temperature, pressure, and wind fields, over ENSO timescales, propagate eastward in a wave train. They named this propagating phenomenon the ''Antarctic circumpolar wave'' (ACW). Peterson and White (1998) suggest that the ENSO signal at Tropics is transferred into the subtropical South Pacific through vertical convection and an overturning cell in the troposphere, and the signal propagates in the ocean over multiple years, to the high latitudes where it becomes a source of the ACW.

Despite these numerous and disparate studies suggesting a link between the polar sea ice fields and global climate (regardless of the linkage mechanisms), the specific nature and significance of how variations in the sea ice fields covary with global or extrapolar climate is still remarkably ill defined. The purpose of this paper is to improve our documentation of such linkages and evaluate their significance, focusing initially on the Antarctic sea ice fields full annual cycle in this study. Specifically, we 1) quantify the variability documented within the Antarctic sea ice fields and isolate primary modes of such variability; 2) identify linear relationships between the sea ice variability and fundamental extrapolar climate modes as well as regional climate elsewhere on the globe; 3) assess the significance of these relationships accounting for space–time autocorrelations; and 4) identify the geographic regions, both within the Antarctic polar region and external to it, that display the strongest links. The identification of global–polar linkages is the first step in determining the mechanisms responsible for such links (the overarching motivation for such studies as this); here we focus on this first step.

2. Data

a. Sea ice data

Satellite measurements of polar sea ice over the last 20 yr have provided typical spatial resolution of 25 km and near daily temporal resolution. These enable us to study variabilities in the sea ice fields from synoptic to interannual timescales. In this study, we use approximately 18 yr (219 months) of sea ice concentration data derived from brightness temperatures measured by the *Nimbus-7* Scanning Multichannel Microwave Radiometer (SMMR; Gloersen et al. 1992) and the Spatial Sensor Microwave/Imagers (SSM/Is). SMMR data cover the period of October 1978–August 1987 with approximately 2-day time resolution, while SSM/I data from three spacecraft (*F8, F11,* and *F13*) cover August 1987–December 1996 at daily resolution. We take advantage of newly recalculated and combined sea ice concentration fields from SMMR and SSM/I sensors (SMMR–SSM/I dataset, hereafter) in which shifts between the different sensors have been minimized, providing a single consistent space–time series (Cavalieri et al. 1997; National Snow and Ice Data Center 1997). This new combined dataset for SMMR–SSM/I data covers October 1978–December 1996.

These data are provided as monthly ice concentration data in 25 km $\times$ 25 km grids that we digitize onto a 0.25° lat $\times$ 1° long polar grid. We then define the monthly mean sea ice edge (SIE) as the equatormost position of the 30% isopleth of ice concentration in each degree of longitude. The SIE is not overly sensitive to the actual isopleth chosen to define it, since the sea ice concentration increases rapidly near ice edge during most of ice-covered season. In austral summer, when 80% of the Antarctic sea ice fields have melted, the ice edge is given as the coastline latitude if no ice is present. Finally, SIE monthly anomalies, SIE′, are generated by subtracting the monthly climatology defined at each degree of longitude (based on the data from 1979 to 1996) from the SIE monthly means. Note that in working with anomaly fields, we are effectively removing the seasonal cycle, as well as any direct signature of stationary standing waves that may be present in the Antarctic circumpolar belt (van Loon and Jenne 1972; van Loon et al. 1973). The use of ice extent information only in the analysis also makes this study basically insensitive to ice concentration values which are known be algorithm dependent (Comiso et al. 1997).

b. Climate data

To investigate teleconnections between Antarctic sea ice and global climate, we use the National Centers for Environmental Prediction (NCEP)–National Center for Atmospheric Research (NCAR) reanalysis surface air temperature at the 1000-Mb pressure level (Kalnay et al. 1996). This variable is in class A of the reanalysis output, which indicates that the variable is most strongly influenced by observed data with minimal model influence. We digitized the NCEP–NCAR monthly mean air temperature (SAT) at 2.5° $\times$ 2.5° grid into a 5° $\times$ 5° global grid from January 1975 through December 1998. Detrended SAT monthly anomaly fields (SAT*) are generated by removing the monthly climatology of SAT at each grid location and then eliminating any trend present in the anomaly at each grid location.

To test the sensitivity of our results to the interpolation or other manipulations unique to the NCEP–NCAR SAT* fields, we repeat a large fraction of our analyses using the Jones's monthly global near-surface temperature anomaly data (Jones 1994; Parker et al. 1994; Parker et al. 1995) and the National Aeronautics and Space Administration GISS global surface air temperature anomaly data (Hansen and Lebedeff 1987; Reynolds and Smith 1994). These latter databases contain large data voids throughout much of the Southern Ocean, whereas the NCEP–NCAR fields provide full

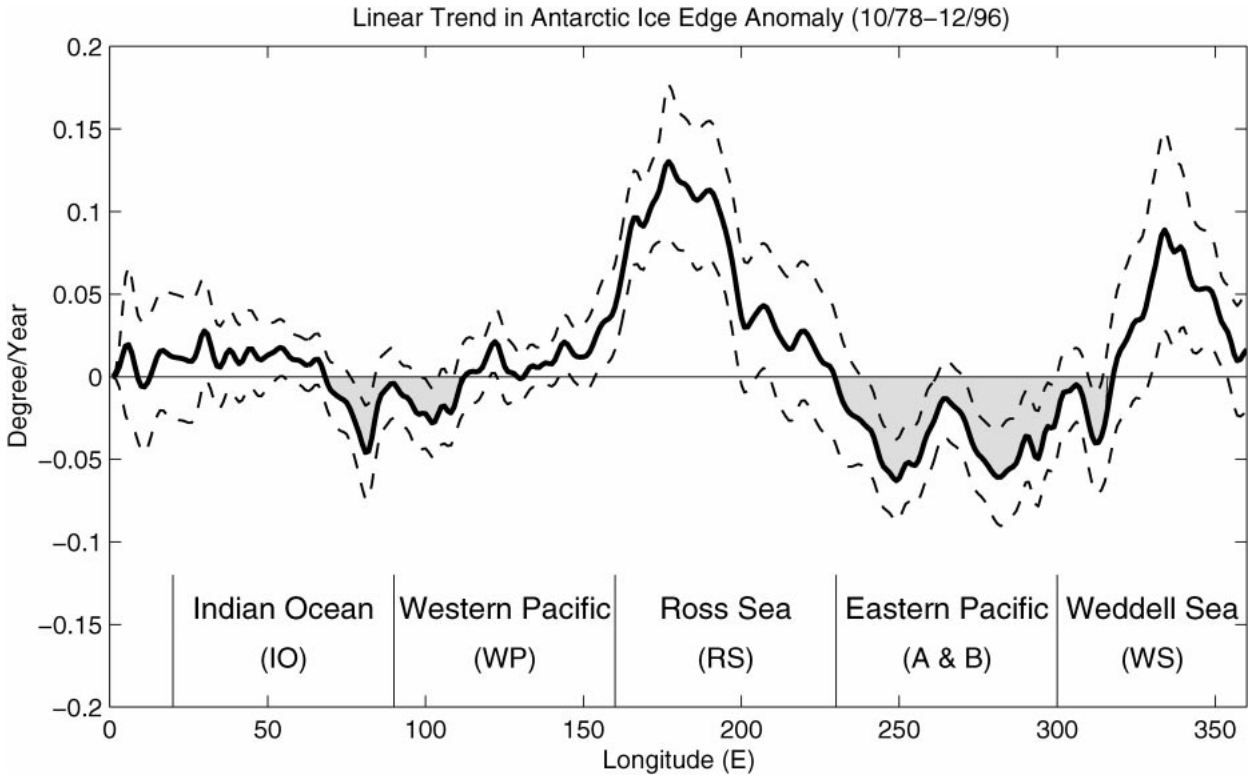

FIG. 1. The linear temporal trend in the SIE′ as a function of longitude (heavy solid line). Dashed lines mark 95% confidence intervals of the trend. The ice edge shows retreat in the shaded areas and expansion in the open areas. Geographic locations are marked. The eastern Pacific region mainly includes the Amundsen Sea and Bellingshausen Sea (A and B).

global coverage. When the NCEP–NCAR SAT* field is subsampled to mimic the spatial coverage of the Jones's and GISS data fields, the principal modes of an empirical orthogonal function (EOF) analysis (presented below) look similar. More importantly, results of repeating the main correlation analysis of section 4 with the different SAT* fields are extremely similar.

Other climate parameters used in the study include an ENSO-related index given by Niño-3 (an eastern equatorial Pacific sea surface temperature averaged in 5°N–5°S, 150°–90°W and robust index for ENSO variability; Cane et al. 1986), a Pacific–North American (PNA) teleconnection index, a North Atlantic oscillation (NAO) index, and a Southern Oscillation index (SOI). These climate indices are provided by the NCEP Climate Prediction Center. In addition, we use a tropical Pacific precipitation index based on station data in the area of 6.25°N–6.25°S, 163.75°E–86.25°W and a tropical non-Pacific precipitation index based on station data in the area of 20°N–20°S, 78.75°W–163.75°E. Both precipitation indices are based on the GISS surface observed land precipitation dataset (Dai et al. 1997) and are generated at the University of Washington's Joint Institute for the Study of the Atmosphere and the Oceans. They are available online (http://tao.atmos.washington.edu/data_sets/). Finally, we generate a tropical Indian Ocean sea surface temperature (SST) index based on Jones's surface temperature anomalies in the area of 2.5°N–12.5°S, 62.5°–82.5°E. The Indian Ocean SST has been suggested to be related to monsoonal intensity (Charles et al. 1997; Kumar 1997).

To focus on interannual (and longer) variability, all time series were temporally smoothed by a Gaussian filter with the filter width of 13 months, to remove variabilities with periods less than a year.

3. Sea ice edge characteristics

The SIE monthly anomaly series (SIE′), that is, after removing the seasonal cycle, contain interannual and longer variability as well as linear trends. A linear regression is applied to the SIE′ as a function of longitude to capture the trends, which are shown in Fig. 1. Averaged around the entire Antarctic continent, the SIE′ displays a net increasing trend of $0.011 \pm 0.043°\ \text{yr}^{-1}$, but with a considerable rms noise level of 0.78°. The result is consistent with the most recent analyses of ice extent trends (Gloersen and Campbell 1991; Weatherly et al. 1991; Johannessen et al. 1995; Cavalieri et al. 1997), though the various studies differ in their assessment of the statistical significance (likely a consequence of the large rms noise which imparts sensitivity to the length of the record being evaluated).

The spatial heterogeneity apparent in Fig. 1 shows

the average trend to be the net consequence of significant spatial variability. Specifically, the most significant ice edge retreat occurs in the Bellingshausen and Amundsen Seas of the eastern Pacific, in agreement with Jacobs and Comiso (1997) and Stammerjohn and Smith (1997; which also contains an excellent review of other sea ice trend analyses and possible mechanisms). Conversely, the ice edge shows equatorward expansion in the Ross and Weddell Seas, which also agrees with Stammerjohn and Smith (1997). For the present study, the trends are removed from the Antarctic SIE′ at each degree of latitude, producing a detrended anomaly SIE series, SIE*.

The spatial decorrelation length of the SIE* field is estimated by calculating the spatial autocorrelation for the spatial series for each month. The mean decorrelation length appears as a function of season with a maximum of 17° longitude in February and a minimum of 5° long in August. The former is clearly dominated by the consistency of the summer SIE. Averaged over 12 months, this yields a decorrelation length of 12° longitude. We therefore choose to average the SIE* into 12° longitude bands to generate 30 quasi–spatially independent time series, ⟨SIE*⟩.

In an attempt to identify coherent spatial–temporal substructure in the SIE*, a complex EOF (CEOF) analysis was applied to identify traveling and standing waves (Wallace and Dickinson 1972; Horel 1984) within the SIE* field. The SIE* time series were filtered by a Butterworth low-pass filter to eliminate noise with periods less than 1 yr prior to the CEOF analysis. The leading mode's spatial pattern (Fig. 2a,b), described by its eigenvector and containing 46% of the total variance, is dominated by two high-variance maxima (of opposite phase): one in the eastern Ross Sea and the other in the Weddell gyre region. The leading mode's temporal variability, as described by its principal component (Fig. 2c,d), has a spectrum similar to that of a pure red noise spectrum generated from integrated white noise (Fig. 2e). However, the mode does display significant spectral peaks (95% confidence relative to 100 realizations of red noise spectra) at frequencies of approximately 1.5–2 yr and just over 5-yr periods. Since the gain function for the Butterworth filter has a smooth transitional band (Roberts and Roberts 1978), the peak with the 1.5-yr period should not be an artifact of the filtering process.

The phase of the first mode eigenvector linearly decreases eastward (except in the Indian Ocean), and the phase of the principle component linearly increases with time, which indicates an eastward-propagating signal. This propagating signal is strongest in the region from the Ross Sea to the Weddell Sea. The principle component reveals a dominate variation with a period of approximately 5 yr. Analysis of the 5-yr component (Fig. 3) shows that it displays an eastward propagation comparable to that of the primary mode. This is consistent with the general filtered characteristics of the ACW (White and Peterson 1996). However, lack of consistent decreasing phase of the eigenvector and relatively lower eigenvector magnitude in the Indian Ocean suggest that no clear propagating signal exists there. The propagating signal either is limited in the Weddell gyre instead of continuously propagating into the Indian Ocean or becomes too weak to detect east of the Weddell gyre. The analysis cannot differentiate between these two possibilities.

Spectral analysis was also applied to the individual SIE* time series at each 12° longitude band. Peaks with periods near 1.5–2 and ~5 yr appear in many longitude bands (Fig. 3). The power within the 5-yr period band is strongest in the western Indian Ocean and central and eastern Pacific. The phase for this band (Fig. 3b) indicates an eastward propagation in the Pacific, though its flat nature in the western Indian Ocean and western Amundsen Sea region suggest that the propagation may be either discontinuous or at different rates in those regions. The power for the higher-frequency band (1.5–2.1 yr) is concentrated in the Weddell Sea and east of the Ross Sea, although this variability does not appear to propagate spatially. This high-frequency interannual variability is consistent with the quasi-biennial oscillation in the Antarctic ice extent suggested by Gloersen (1995).

The spatial pattern of the second mode (not shown), which contains 16% of the total variance, captures the nonconcentric asymmetry of the Antarctic sea ice fields. That is, the ice shows enhanced variability in the regions most equatorward in the central Pacific and western Indian Ocean. This pattern is particularly strong during the period 1987–1989.

4. Global connectivity

a. Tropical climate links

We first explore connections, in the form of linear correlations, between the Antarctic sea ice fields and the general climate indices described in section 2b. Although the tropical indices (Niño-3, SOI, Indian Ocean SST, and Pacific precipitation indices) covary to some extent, they do represent different aspects of tropical climate variability and contain considerable unrelated variance between them as well (typically 50% or more, with maximum shared variance always occurring at zero lag). The strongest correlations (Fig. 4) involve the ⟨SIE*⟩ over wide bands of the eastern Pacific and western Weddell gyre regions, and the Indian Ocean SST, Pacific precipitation, and Niño-3 indices. Correlations with the other indices do not reveal consistently strong correlation patterns. The maximum correlation between ⟨SIE*⟩ and NINO3 is $r = 0.58$ (r denotes correlation coefficient) at 1-month lead, implying that ~34% of variance in the ⟨SIE*⟩ is linearly related to that in ENSO. The tropical Indian Ocean SST and Pacific precipitation generally show even higher correlations to ⟨SIE*⟩ than the Niño-3 index. The maximum correlation coefficient

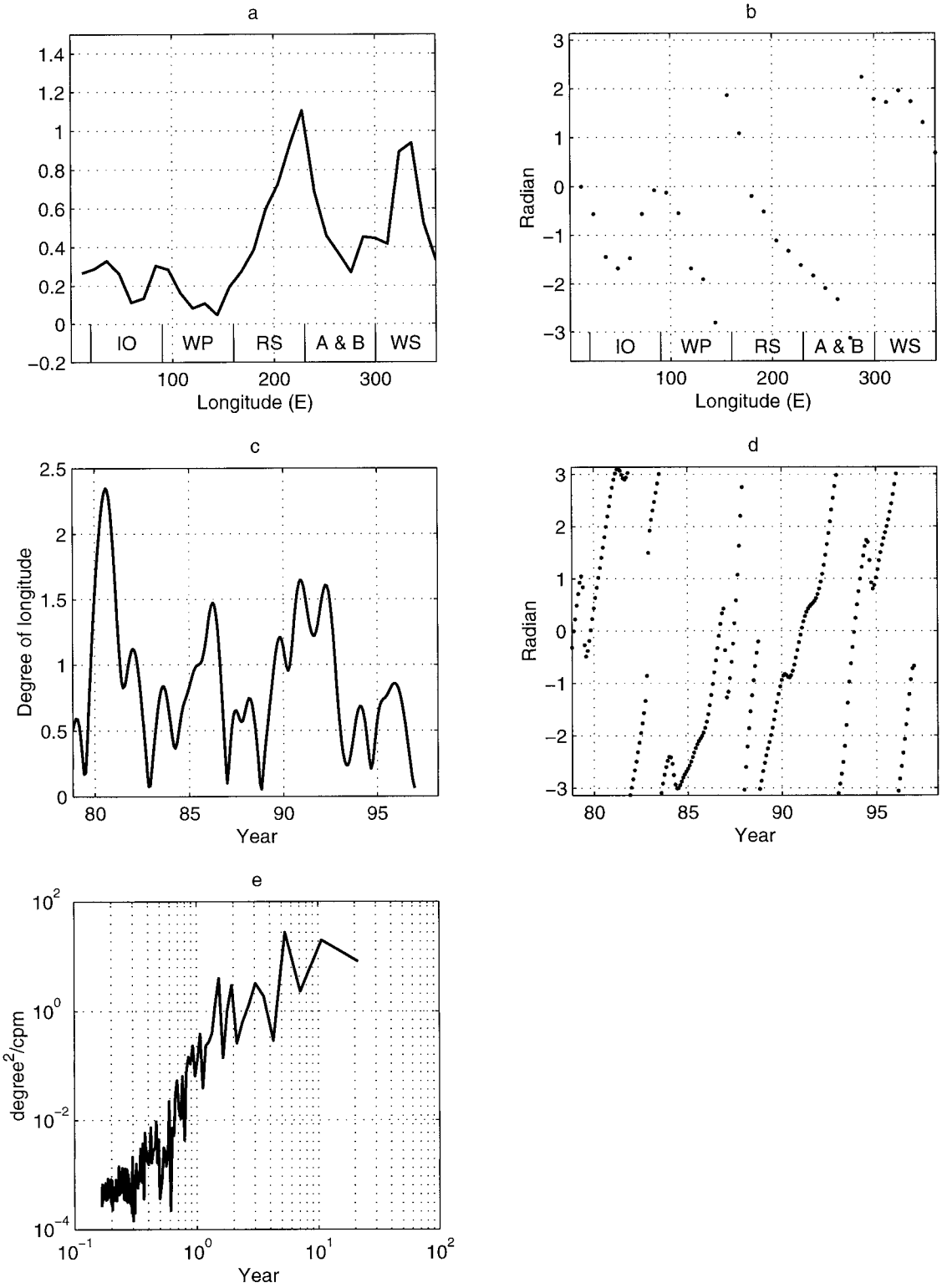

FIG. 2. Leading mode of the ⟨SIE*⟩ at 30 12° longitude bands given by a complex empirical orthogonal function analysis: the (a) amplitude (b) phase of the eigenvector as functions of longitude, the (c) amplitude and (d) phase of the principal component as functions of time, and the (e) power spectrum of the amplitude of the principal component.

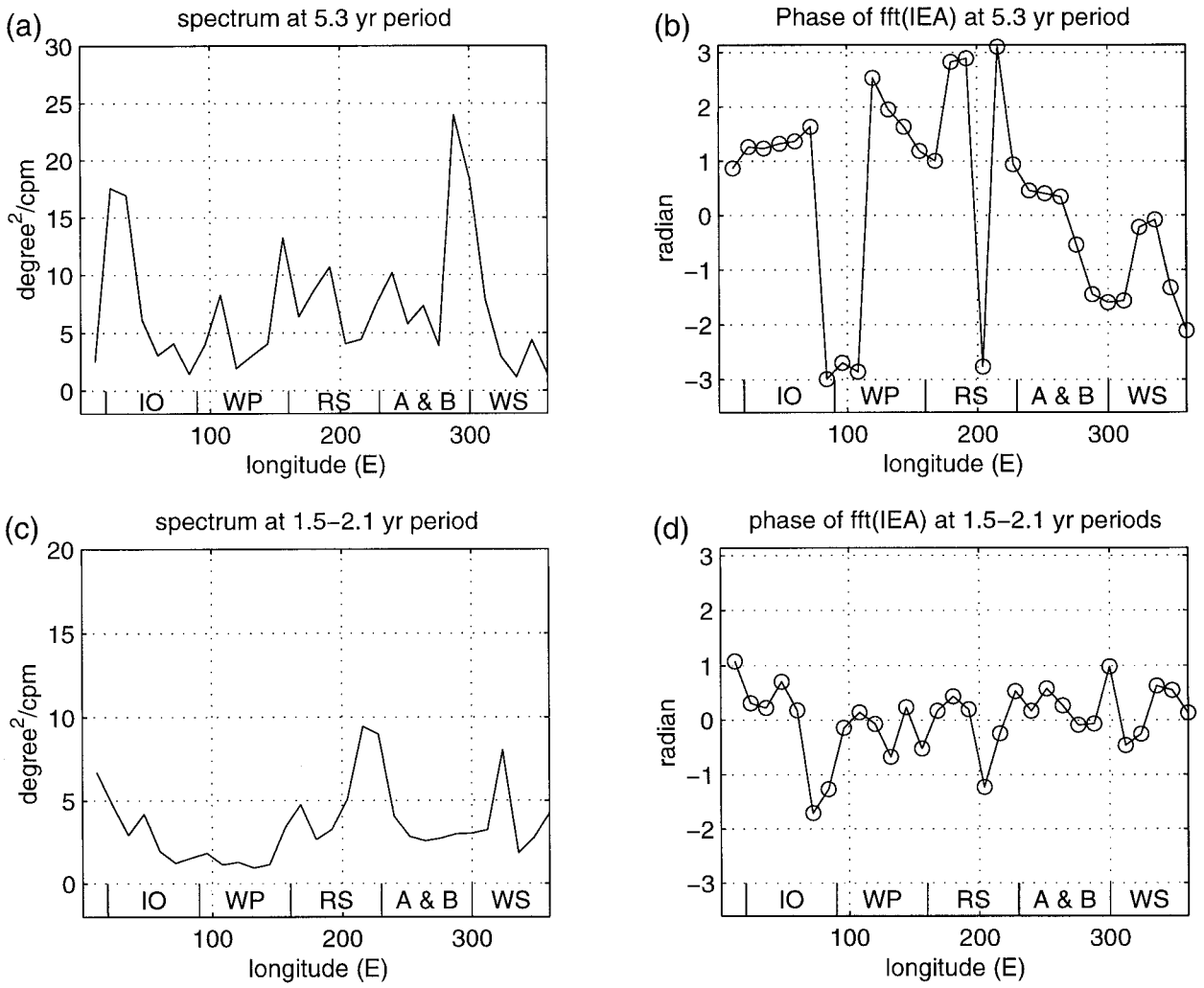

FIG. 3. Spectral amplitude of ⟨SIE*⟩ as function of longitude at the (a) 5.3-yr period and (c) 1.5–2.1 yr periods. The phase of the Fourier transform is plotted for the (b) 5.3 yr period and (d) 1.5–2.1 yr periods.

reaches 0.69 at 2-yr lag and 0.65 at 3-month lead for the tropical Indian SST and tropical Pacific precipitation, respectively.

The correlation structure in Fig. 4 reveals a coherent propagating pattern that manifests itself as a series of diagonal correlation bands (from the upper left to lower right of the correlation matrices). The specific regional area within these bands that show the highest correlations with the climate indices changes as a function of increasing time lag from west to east. For example, one of the areas with strongest correlations at zero time lag in Fig. 4c involves the ⟨SIE*⟩ in the westernmost Amundsen Sea (~240°E). With increasing time lag the area of peak correlation then migrates to the east at a rate of approximately 45° yr^{-1}. The peak correlation makes one complete rotation around the Antarctic in approximately 8 yr, with peak correlations appearing consistently in the eastern Pacific Ocean and western Weddell gyre region. In the former region, it migrates from the western Amundsen Sea to the tip of the Antarctic Peninsula in approximately 24 months. This eastward migration speed is consistent with the phase propagation speed of the ACW (White and Peterson 1996).

The diagonal patterns also extend into positive lag regions, suggesting that changes in ⟨SIE*⟩ presage changes in extrapolar climate. However, the eastward migration of peak correlations across positive and negative leads reflects both a spatially coherent structure in the ⟨SIE*⟩ as well as the quasiperiodic nature (at 1.5–2- and ~5-yr periods) of the ⟨SIE*⟩ and climate indices. Since we do not know the mechanistic sense of the correlative relationships (assuming them to represent causal links), we cannot differentiate in a physical sense the lead–lag relationships between ⟨SIE*⟩ and climate indices. Regardless, for present purposes, the results show a considerable degree of covariability between

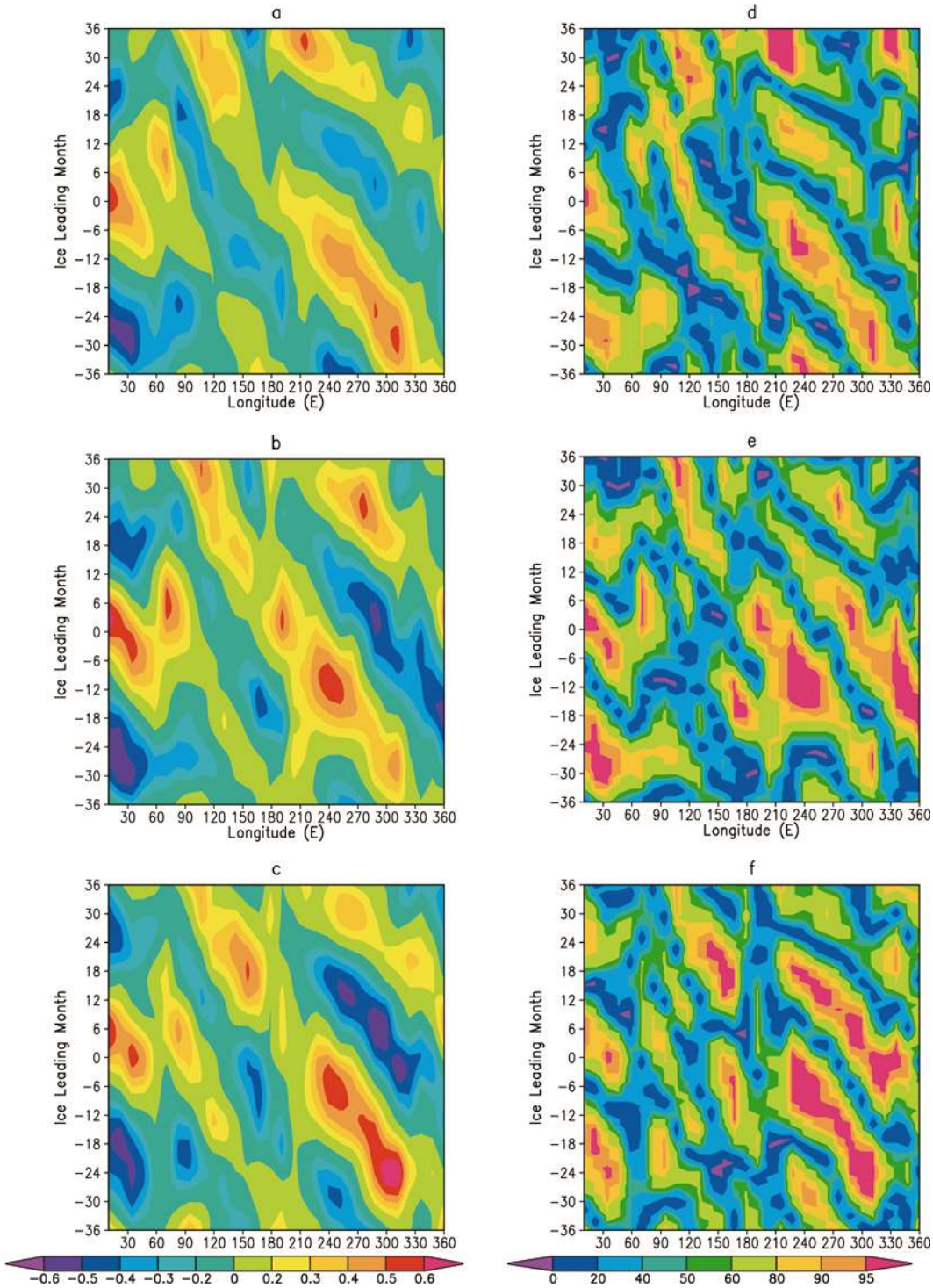

FIG. 4. Cross correlations (with lags of ≤|3| yr) between ⟨SIE*⟩ and (a) Niño-3, (b) tropical Pacific precipitation, and (c) tropical Indian Ocean SST. (d), (e), and (f) Local confidence levels for above correlations. The SIE was averaged into 12° longitude bands to generate near-independent datasets, prior to the correlation. See Fig. 1 for geographic locations of longitudes.

⟨SIE*⟩ and extrapolar climate indices, and strong spatial coherency of the relationships with an eastward propagation consistent with the phase speed of the ACW.

For the time series used in this analysis, a cross correlation of $|r| > 0.2$ would be significant at 95% confidence level if all of the data points in the time series were independent. However, the monthly values are not independent, and their degree of autocorrelation dictates that, for most cases, a correlation of $|r| > 0.5$ is significant at the 95% confidence level. There are a few time series where correlations at the 0.5 level are significant at just under 95% confidence, and others where they are better than 95%, but these are subtle differences affecting a minority of series. Also, correlations involving the tropical Indian Ocean SST and Pacific precipitation yield slightly higher confidence levels for the same r value as those involving Niño-3 since the latter has a higher degree of autocorrelation. All of these factors are taken into account in the confidence levels of Fig. 4. More detailed discussion on the significance tests of these linear correlations is given in the appendix.

b. Links with global surface temperature

While the above correlations suggest that a considerable fraction of the variance of the ⟨SIE*⟩ appears to be linked to tropical climate variability, as measured by the climate indices, here we investigate the spatial–temporal distribution of polar–global climate links. Initially this is done by computing linear correlations between the ⟨SIE*⟩ and global SAT anomaly series (SAT*) described in section 2. Since the mean temporal decorrelation length of the ⟨SIE*⟩ series is about 6 months, the correlations are computed at half-year lag intervals up to ± 2 yr, generating a total of 270 global correlation maps. The confidence level at which the correlation in every grid cell is significant is calculated using an effective degrees of freedom, as described in the appendix. Since this confidence level only takes into account the temporal autocorrelation within the ⟨SIE*⟩ and SAT* series and does not consider spatial coherence within the SAT* field, we consider it the ''local'' confidence level. The spatial coherence is tested separately via use of statistical field tests described in the appendix. It is also considered through EOF analyses later in this section.

Before attempting to distill physically meaningful results or regional links from the numerous correlations, we first performed a number of tests to assess their statistical significance. The tests were designed to determine if the results yield more statistically significant (at the 95% confidence level) correlations around the globe than expected by simply correlating the global SAT* series to noise displaying the same general spectral coloring as the ⟨SIE*⟩ series. We do this by conducting 1) local significance tests that take into account the effect of temporal autocorrelations present in the datasets being correlated, and 2) field significance tests that take into account the spatial coherence (spanning all scales) inherent in the SAT* data. The details of these tests and their results are described in the appendix; they are summarized here for convenience. Finally, we apply the concepts of multiplicity to determine which of those correlations exceeding that expected from simple correlations to noise are most likely to represent the physically meaningful ones.

Briefly, the statistical tests show that correlations of ⟨SIE*⟩ with global SAT* reveal considerably more (almost twice as many) significant correlations than expected by correlating the SAT* with noise containing the same spectral coloring as the ⟨SIE*⟩ data. Specifically, on average approximately 4% (mode value) of the global grid will yield correlations significant at, or above, the 95% confidence level if we correlate colored noise to the SAT*. Instead, using the ⟨SIE*⟩ data, more than 8% of the global grid, or twice as much, yields significant correlations on average (i.e., for any particular lag or ⟨SIE*⟩ series). When comparing means, the result is more than 9 standard deviations beyond the mean expected for the quasiperiodic colored noise. Furthermore, there is a large band over which the data show considerably more significant correlations than the noise shows. That is, for significant correlations covering more than 6% of the global grid, we find considerably more (nearly twice as many) results in this band than would be expected from correlations with quasiperiodic colored noise.

Of the correlation fields, 65% of the results yielding higher number of significant correlations than expected (at the 95% confidence level) occur for cases in which ⟨SIE*⟩ leads (from 6 to 24 months) changes in SAT*. An additional 13% occurs for zero-lag cases. However, these results are fairly sensitive to subtle changes in the time series being correlated (e.g., removal of a year of data from the ⟨SIE*⟩ time series changes this result significantly). These results are also biased somewhat, though not completely, by high southern latitude relationships reflecting a regional influence of ⟨SIE*⟩ on SAT*; if the SAT* fields south of 50°S are removed from the correlations, the correlations are more evenly distributed between positive and negative lags. Consequently, we cannot claim any physical significance (at least outside the Southern Ocean region) to these percentages at present, and as with the climate indices, the physical implications of lead–lag relationships in correlations are meaningless without a clear understanding of the mechanisms responsible for the links.

Likewise, while the considerable degree of significant correlations is a highly robust finding, we cannot distinguish which regions yielding significant correlations represent likely physical links from those that can be expected to arise from correlations with noise. However, here we can perform additional analyses in an attempt to identify spatial correlation patterns that are consistent with spatial distributions of known climate phenomena, and therefore likely links to those phenomena. We es-

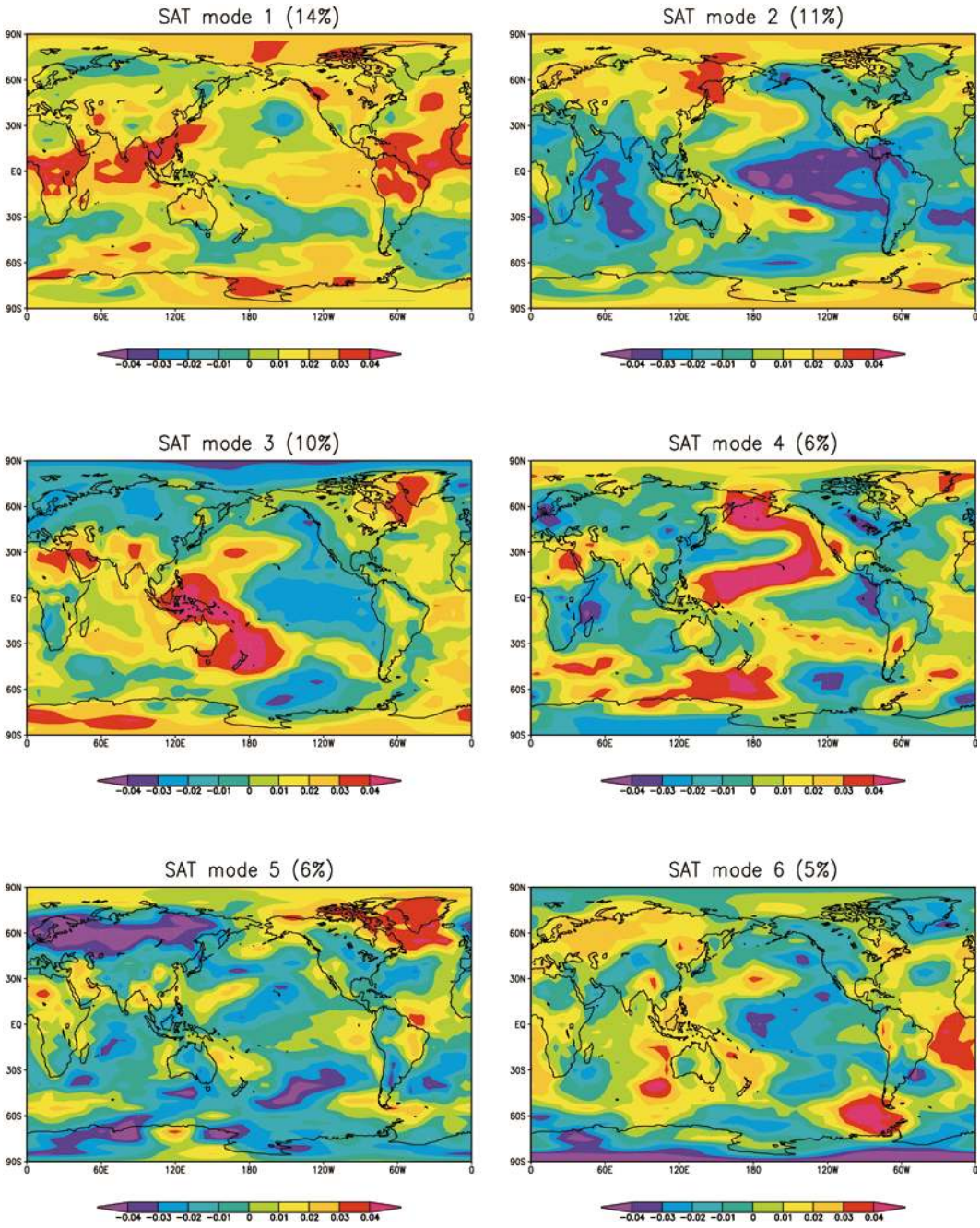

FIG. 5. Leading modes eigenvectors for NCEP–NCAR reanalysis surface air temperature anomalies from 1975 to 1998.

tablish the spatial patterns through an EOF analysis of the SAT* global data (decomposing the locally normalized and detrended SAT correlation matrix). The first six modes are shown in Fig. 5. Though not clearly separated, the first three modes, representing 14%, 11%, and 10% of the total variance, respectively, reveal distinct spatial patterns that seem to capture 1) a considerable segment of the tropical Atlantic and Indian Oceans, as well as neighboring continents; 2) the tropical Pacific ENSO pattern (Rasmusson and Carpenter 1982), including much of the central Indian Ocean; and 3) the western extreme of the tropical and southern Pacific Ocean. Thus, while these modes may not represent true dynamic modes of the climate system, they are a reasonable attempt at isolating global modes that may have physical significance given their spatial coherence.

Spatial patterns dominating these low-order modes are often captured to some extent by the spatial distri-

bution of significant correlations, as seen in the correlation maps. For example, four correlation maps, presented with their local significance (see appendix for statistical assessments), are presented in Fig. 6. These highlight the principal patterns that recur throughout the correlations, and which are often present to some degree in the modes.

The global correlations involving ⟨SIE*⟩ between 0° and 12°E at zero lag (Fig. 6a), display many of the same spatial characteristics as seen in modes 2 and 3 of Fig. 5. In particular, high correlations capture the eastern Pacific portion of the ENSO pattern in the Pacific, while some strong correlations ($|r| > 0.5$) are present in the Indian Ocean and North Atlantic–North America region. This is somewhat consistent with the observation that the SST anomaly in the central Indian Ocean is in phase with the tropical Pacific SST during the peak phase of El Niño, although the magnitude of the anomaly is usually smaller in the Indian Ocean than in the tropical Pacific (Kawamura 1994; Tourre and White 1995). However, the correlation with ⟨SIE*⟩ at 0°–12°E shows the same or even more shared variance with the Indian Ocean SST as in the Pacific, suggesting a stronger affinity with the Indian Ocean component of the ENSO phenomenon. Note that the local confidence levels in the tropical Pacific are lower than in the Indian Ocean and North America because of higher autocorrelation in the tropical Pacific SST. In the Indian Ocean and North America, the correlations that are larger than 0.4 are locally significant at the 95% confidence level. However, not all correlations in the tropical Pacific that are larger than even 0.5 are locally significant at the 95% confidence level. In addition, a similar correlation pattern but with opposite sign appears when the 0°–12°E ⟨SIE*⟩ series leads and lags SAT* by 2 yr—about half the period of the eastward-propagating ⟨SIE*⟩ signal. Moreover, this correlation pattern frequently appears when ⟨SIE*⟩ in the eastern Atlantic and eastern Pacific is correlated with the global temperature. When ⟨SIE*⟩ at the eastern Weddell Gyre leads by 6 months, high correlations are concentrated in the Indian Ocean.

Figure 6b presents the correlation map involving ⟨SIE*⟩ between 72° and 84°W at zero lag. This map captures the western–central Pacific ENSO pattern and much of its high-latitude pattern signature (as seen in mode 3 of Fig. 5, but also in modes 5 and 6). The negative relationship between the western–central Pacific and the region around the Antarctic Peninsula is particularly strong in this correlation field. This is consistent with earlier findings that have linked ENSO with this region of the Antarctic (e.g., Simmonds and Jacka 1995; Smith et al. 1996; Peterson and White 1998). When ⟨SIE*⟩ at the western Weddell gyre leads 12–18 months, correlation fields show the same pattern.

The correlation maps in Figs. 6c and 6d both involve ⟨SIE*⟩ between 120° and 132°W, but the former map is for zero lag while the latter is for ice lagging SAT* by six months. Both correlation maps show considerable linkage between this Amundsen Sea region of the Antarctic and the central–eastern Pacific and western Indian Ocean–Africa signature of ENSO and mode 1 of Fig. 5, as well as with a meridional banding structure running the full extent of the North and South Atlantic. The magnitude of the extrapolar correlations are strongest when ⟨SIE*⟩ lags SAT* by 6 months, which indicates that a boreal fall–winter El Niño event, for example, would have a corresponding signature in ⟨SIE*⟩ 6 months later during early ice growth in the austral fall–winter. Note that there is no similar correlation pattern for this 120°–132°W ⟨SIE*⟩ band in cases where the ⟨SIE*⟩ leads SAT*. Both correlation maps show a very strong Antarctic dipole between the Amundsen Sea and Weddell Sea regions, with this structure strongest at zero lag. In addition, the Antarctic dipole pattern repeatedly appears when ⟨SIE*⟩ in the eastern Pacific and Weddell Sea is correlated with the global temperature. The meridional banding structure is frequently found in the correlation fields with ⟨SIE*⟩ at the eastern Pacific region of the Antarctic.

In an attempt to distinguish signal from noise, a difficult task, we performed an EOF analysis on those correlation maps that showed significant correlations covering more than 6% of the global grid. This is the band for which the data showed considerably more significant correlations than expected from the quasiperiodic colored noise, and therefore, the EOF modes should reveal the primary geographic distributions of teleconnections most likely to represent signal, unique to the data (though this will still contain some of the links expected through noise). While this is not a rigorous test, it should at least provide a first pass at focusing attention on those global correlations most likely representative of physically meaningful signal.

The first six modes of this analysis are shown in Fig. 7. The first two modes clearly display many of the spatial patterns captured in the first few SAT* modes of Fig. 5, but there are also a number of patterns here that seem to reflect the unique nature of the polar–extrapolar relationships. Most notable is the strong Antarctic dipole, noted above, and the Atlantic banding structure that is apparent in several of the maps presented in Fig. 6. There is also a persistent link between the ice at several locations around the Antarctic and the Indian Ocean in general.

While the previous statistical assessments showed that there are nearly twice as many polar–extrapolar significant correlations than would be expected from correlations to quasiperiodic colored noise, we must invoke the concepts of multiplicity (Katz and Brown 1991) in order to best estimate which of these significant correlations are likely representative of a physically meaningful link. That is, half of the significant correlations are expected from noise, and the other half presumably represent signal, but without multiplicity tests we cannot differentiate which of these likely represent the latter. Multiplicity deals with the problem whereby

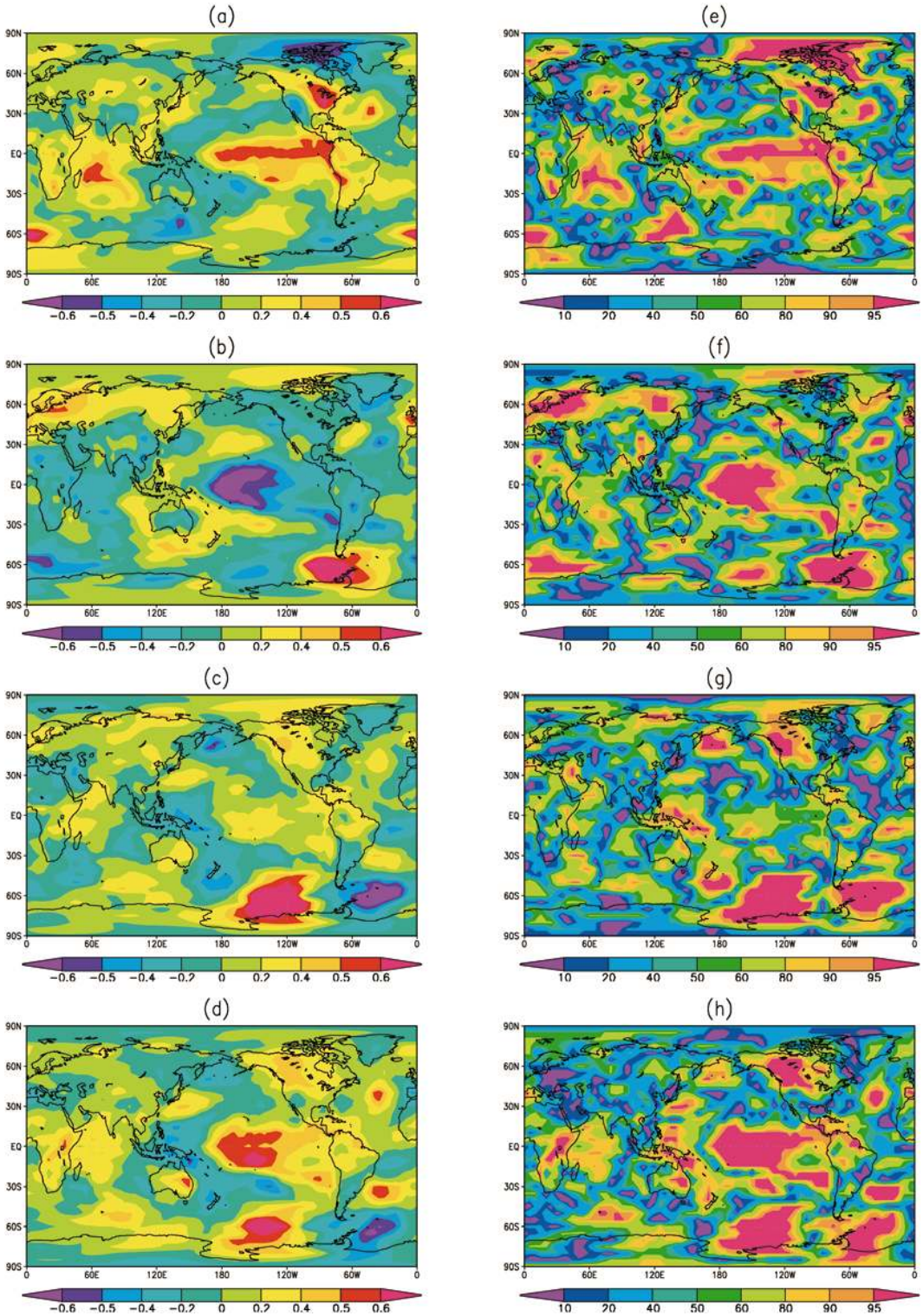

FIG. 6. The linear correlation between NCEP–NCAR surface temperature anomalies and (a) ⟨SIE*⟩ at 0°–12°E with zero lag, (b) ⟨SIE*⟩ at 72°–84°W with zero lag, (c) ⟨SIE*⟩ at 120°–132°W with zero lag and (d) ⟨SIE*⟩ at 120°–132°W when ⟨SIE*⟩ lags by 0.5 yr. (e), (f), (g) and (h) The corresponding local confidence levels.

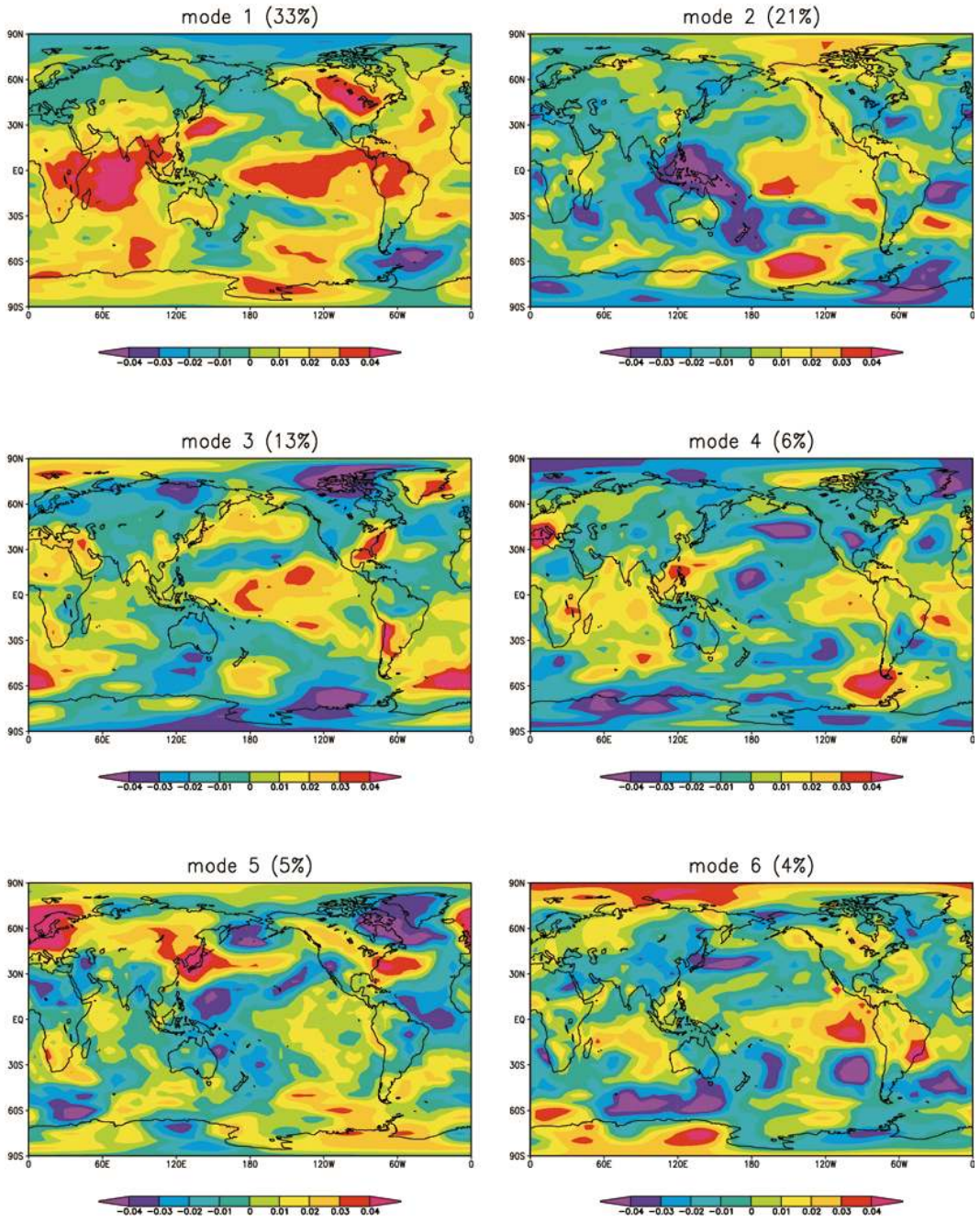

FIG. 7. Leading-mode eigenvectors for correlation fields generated by correlating 30 ⟨SIE*⟩ and NCEP–NCAR global surface air temperature anomalies at half-year lag intervals up to ±2 yr.

the more correlations computed, the higher the likelihood that some will pass as significant even when they are not. Katz and Brown (1991) discuss the problem and provide equations for compensating the level of significance when using a high number of correlations. Adjustments must be made for the degree of spatial and temporal autocorrelation. Katz and Brown (1991) assume a specific form of autocorrelation in time, which may or may not be appropriate in the present study. However, the net consequence of multiplicity is that the minimal *r* value required to show significance at a 95% confidence level for an individual test must be elevated higher to yield the same confidence level when computing multiple correlations. Therefore, in the correlation maps where 8% of the globe showed significant correlations, the 4% of this coverage that is most likely to reflect a physically meaningful link, as opposed to the other 4% expected by correlating to noise, must lie

with those areas showing the largest *r* values. Indeed, when isolating the highest *r* values, they tend to cluster in those areas highlighted in the EOF analysis of Fig. 7. In particular, the highest *r* values appear in the areas of the first four EOF modes of Fig. 7.

Finally, to test the sensitivity of our results to the specific SAT* fields employed, we repeated the correlations using the SAT* fields derived from the Jones (1994; Parker et al. 1994; Parker et al. 1995) and GISS (Hansen and Lebedeff 1987) surface air temperature databases. When the NCEP–NCAR SAT* fields are subsampled to provide the same spatial coverage as the GISS and Jones SAT* fields, the results of the correlations and EOF analyses are extremely similar, though obviously we lose patterns linked to the high southern latitudes due to the data void in the Southern Ocean.

5. Discussion

We have sought to determine if there was clear evidence of interannual physically meaningful links between the Antarctic sea ice extent and extrapolar climate. Our results suggest a high probability that a significant fraction of the links identified here (representing approximately 8%, on average, of the global surface area) are not just a consequence of red noise, or even quasiperiodic noise. This implies a significant meridional communication between the polar and extrapolar regions. Clearly we do not yet understand the mechanisms that might lead to such far-reaching meridional teleconnections. In fact, it is our hope that by identifying the explicit nature of the persistent regional ties, they may provide a suitable diagnostic against which climate models can be gauged, and eventually serve as a focal point through which the models can be evaluated to help identify the underlying mechanisms.

In the meantime, we offer a brief summary of previous studies in which polar–extrapolar links have been identified and for which a variety of potential mechanisms have been suggested. We find that these studies fall into two general categories: 1) those that have focused on identifying the links (as is the case of this study), and for which mechanisms presented are done so in a rather speculative manner; and 2) those that have explicitly sought to identify and understand the mechanisms of the polar–extrapolar meridional teleconnections. The vast majority of the studies fall into the first category, though the insights they provide, in combination with the insights from the second category begin to provide a general picture of the most fundamental means of communication.

Many of the previous studies focused on and found a relationship between the Antarctic and the Southern Oscillation (which we represent with Niño-3 in this study), or with ENSO in general (e.g., Mo and White 1985; Smith and Stearns 1993; Simmonds and Jacka 1995). Much of this undoubtedly stems from the fact that Walker (1923), who first coined the phrase ''Southern Oscillation'' (Walker 1924), suggested that it may be of Antarctic origin. Chiu (1983) used early, and sparse, data to show that a relationship existed between the SOI and Antarctic sea ice, with changes in the sea ice leading those in the SOI [consistent with Walker's (1923) premise]. Chiu (1983) attributes this relationship to the fact that the pack ice is related to Southern Ocean cyclonic activity (Schwerdtfeger and Kachelheffer 1973) and to surface winds (Streten and Pike 1980); the winds are related to the surface pressure field, which is organized in a large-scale pattern through the Southern Oscillation (though he notes that the SOI itself is not as important as the large ''sloshing'' back and forth of the pressure extremes between continental loci, as described by Julian and Chervin 1978). While no specific mechanism is offered, the relationship between sea ice, winds, and pressure is implicated. Chiu (1983) also notes that we might expect a seasonal dependency on the relationship, as the physics controlling the nonseasonal variations may be seasonally dependent.

Krishnamurti et al. (1986), in a study of low-frequency pressure anomalies and their role in ENSO cycles, traced atmospheric pressure anomaly patterns to show that major pressure reversals over the Indian Ocean and eastern tropical Pacific, preceding El Niño events, can be traced to meridional migrations of pressure anomalies from the south polar regions to the north polar regions during one decade and from the north polar regions to the south polar regions in the ensuing decade. While they offer no mechanism for the meridional migration of the pressure anomalies, they did estimate that the pressure anomalies were of sufficient magnitude to induce changes in the equatorial boundary layer winds to generate the westerly wind anomalies associated with El Niño events once the anomalies migrated to tropical latitudes. Krishnamurti et al. (1986) also find a wavenumber-3 pressure pattern that makes a polar oscillation with two to three waves in any one location during a decadal period that gives rise to the pressure changes observed on timescales of the Southern Oscillation. The timescale of this polar oscillation is similar to that of the wavenumber-2 ACW of White and Peterson (1996). Krishnamurti et al. (1986) do not invoke sea ice in their discussion and also note that the absence of data between 50° and 70°S (the sea ice zone) is a major limitation in their analysis. However, we note that periods of anomalous low pressure in the sea ice zones should coincide with enhanced surface divergence and thus the potential for more equatorward expansion of the sea ice. This appears to be borne out by the analysis of Carleton (1988) who, in a case study of the relationship between the Weddell Sea pack ice and the Southern Oscillation, found that enhanced cyclonic circulation in the Weddell gyre region led to equatorward expansion of the sea ice, and the opposite for anticyclonic anomalies.

More recently, Simmonds and Jacka (1995), using a much better sea ice dataset than available for Chiu (1983), showed a strong (seasonally dependent) rela-

tionship between the sea ice extent and SOI, though in this case, the sea ice typically lagged the changes in SOI, though they do report that the larger correlations of the sea ice to the west of the Ross Sea with SOI involve the sea ice leading SOI. For the zonally averaged case, the relationships are dominated by ties to the Indian Ocean sector of the sea ice fields. There is also good correlation with SOI and the Pacific springtime sea ice. There is little to no relationship between SOI and the Atlantic sea ice. Simmonds and Jacka (1995) point out that the relationships, which show considerable space–season variability, can be confounded if seasons are not selectively isolated and analyzed separately. Consequently, the correlations we find in the present study, at least with regard to ENSO phenomena, may be degraded by considering the entire annual monthly values in all of the correlations. Finally, while Simmonds and Jacka (1995) do not invoke any mechanism for their observed relationships, they do mention the modeling findings of Meehl (1991; discussed below), and they give a good review of the literature presenting various mechanisms that might allow a sea ice–extrapolar climate link. Mechanisms involve the influence of the sea ice extent on the strength of the westerlies and from that, the implication of broader influences (e.g., Simmonds and Wu 1993), and the influence of the sea ice on the surface pressure field, including the tropical pressure fields (Simmonds and Dix 1986; Mitchell and Hills 1986).

From another perspective, a number of investigators have examined the relationship between the semiannual oscillation (SAO) and sea ice, which also lends insights to the mechanisms through which the sea ice and extrapolar regions may communicate. The SAO was originally described by Reuter (1936) and then again more thoroughly in the early 1960s by Schwerdtfeger (1960, 1962). It is a highly variable feature of the annual cycle of pressure and meridional temperature gradient (van Loon 1972), appearing in the latter as two equinoctial maxima in the midtropospheric temperature contrast between mid- and high latitudes of the Southern Hemisphere (van Loon 1967).

Van Loon (1967), in discussing the origin of the SAO, indicates how the polar–extrapolar contrasts, including those involving sea ice distribution and upper-ocean structure (through its heat balance), can influence this predominant feature. Specifically, meridional asymmetries in the surface and midtropospheric heating rates arise through the seasons as the amount and local influence of incoming solar radiation changes with latitude and continentality. The former delays the seasonal minimum temperature in the polar regions relative to the northern latitudes since the absence of winter solar radiation results in the prevailing outward radiation determining the seasonal march of temperature. This leads to a maximum in the mid- to high-latitude meridional temperature gradient. The gradient is further enhanced since the polarward flowing advected air masses become cooler as they must originate from waters that continue to cool with the approach of winter and that appear increasingly to the north as the sea ice advances. A reverse situation (with some notable differences) occurs with the transition to summer. Consequently, the meridional temperature gradient is maximum in the transitional seasons, which leads to a strengthened and more equatorward circumpolar trough, and a more southerly and broader trough in winter and summer, thus influencing one of the more prominent features of the Southern Hemisphere circulation and level of cyclonic activity. The relationship between the subtropics and Antarctic subpolar region (including the effects of sea ice) in cyclone activity has been documented by a number of researchers (e.g., Orlanski et al. 1991; Godfred-Spenning and Simmonds 1996).

Key to this polar–extrapolar interaction is an asymmetry in heating in spring and cooling in fall due to the capacity of the surface layer to store heat, and thus offset the timing of warming and cooling associated with the solar cycle. Here the sea ice is particularly important since a deep winter mixed layer in subpolar regions can sustain considerable ocean heat loss over long periods (sustained by the constant deepening of the surface layer), but the summer warming will come unusually quickly due to the thin stable surface melt layer that forms in spring. This imparts a strong seasonal asymmetry in subpolar regions that is not present in the extrapolar waters that do not undergo a seasonal sea ice cover. Van Loon (1967) also notes that as the circumpolar trough shifts, differences in pressure between land and sea areas of the Southern Ocean region amplify the mean wave pattern, strongly influencing the advection of poleward air masses. This amplification may also have influences on and feedbacks with the distribution of the sea ice fields.

Simmonds and Jones (1998) report that the SAO in high latitudes is strongest near the Ross Sea, where we find some of the stronger ties with extrapolar climate. It was originally thought to be a predominantly sub-Antarctic feature, but van Loon (1984) showed that a critical time in the evolution of an extreme in the Southern Oscillation coincided with the time of year when the SAO was in its most equatorward position. The SAO has also been documented in the extratropics (Large and van Loon 1989; Trenberth et al. 1990). In midlatitudes it is greatest in the central Atlantic and Indian Oceans. The former is one link that does not show up as much in previous studies of the sea ice and extrapolar links.

A number of studies have presented general concepts and early model results that suggest a mechanistic link between the polar and extrapolar regions. Of these, the comprehensive studies of Fletcher (1969) and Walsh (1983) are two of the earliest and best. Of the studies more explicitly addressing the mechanisms, James (1988) put forth a hypothesis whereby Rossby waves, forced at high latitudes, propagate into the low and midlatitudes. James (1988) was striving to understand the

mechanisms responsible for generating the high-amplitude steady planetary wave structure of the Southern Hemisphere circulation revealed by van Loon and Jenne (1972) and Trenberth (1980), among others [including most recently, the work of Thompson and Wallace (1998), which approaches this from a slightly different perspective]. He found that asymmetries in their structure arise from the geographic disposition of the Antarctic continent and its thermal forcing, zonal variations in SST (affected by sea ice), as well as the more often considered orography. While not explicitly addressing the role of sea ice, James (1988) did show how effective the high-latitude Southern Hemisphere was in generating long-wavelength Rossby waves that could influence the extrapolar regions. These results appear to be consistent with more recent modeling work done by Hines and Bromwich (1999). James (1988) also noted how the persistent Antarctic surface drainage (Parish 1984) influences the strength of the polar vortex by driving upper-level convergence, which in turn influences the larger-scale forcing. More recent work by Simmonds and Law (1995) suggests that the relationship between katabatic winds and strength of the upper-level flow may be more complex but still finds some relationships. Since the katabatic winds may also be sensitive to the land–sea [and thus sea ice; e.g., Parish (1992)] conditions near the continental coast, it is possible that changes in sea ice concentration (related to divergence and thus to ice extent in the simplest sense) may also influence this upper-level flow, though this is speculation.

White et al. (1998) have examined mechanisms for maintaining the ACW, which involve a feedback between anomalous meridional Ekman heat advection and anomalous turbulent heat flux loss to the atmosphere, but they are not sure of the mechanism by which the extrapolar region communicates with the polar region. They suggest an atmospheric connection via quasi-stationary Rossby waves, suggested by Karoly (1989). Peterson and White (1998) also suggested an oceanic connection with a 4-yr lag time, which, if true, could account for long lead–lag associations between the sea ice and tropical indices.

Meehl (1991) explicitly addressed the mechanisms associated with the SAO. He finds that, consistent with the original hypothesis of van Loon (1967), the SAO is a consequence of different annual cycles of temperature between the Antarctic polar continent and midlatitude polar oceans. While he does not explicitly address the role of sea ice in this study, it again points to a mechanism by which the meridional thermal gradients can lead to polar–extrapolar communications. Since the sea ice may be expected to play a role in this gradient, changes in its extent (and concentration) may thus be expected to influence the meridional exchange as well.

Peng and Wang (1989) use a model to suggest that the observed correlation between the Antarctic sea ice areal extent and strength of the northwest Pacific subtropical high is due to a large-scale teleconnection whereby an anomalously large sea ice area and extent leads to colder westerlies and underlying ocean currents, leading to a sequence of colder currents progressively equatorward until ultimately the Walker circulation is strengthened and the Hadley circulation weakened, leading to a weaker northwest Pacific high (or vice versa for a decreased ice area). Bromwich et al. (1998) also show that changes in sea ice concentration influence the Hadley circulation, but contrary to Peng and Wang (1989) they find that the equatorward propagation of the polar signal is along the western Pacific, consistent with James (1988).

Finally, communications between the Arctic polar region and extrapolar region is accomplished via changes in the pressure fields associated with the Arctic oscillation (Thompson and Wallace 1998) or NAO (see Hurrell 1995). However, this may be facilitated by the more meridional structure imposed by the land–sea distribution that essentially opens a corridor through the North Atlantic into the Arctic.

The above studies suggest that polar–extrapolar communications can be influenced by changes in the polar pressure, surface winds (particularly the westerlies), and temperature fields, through a number of seemingly disparate means. While many of those studies involve these fields over the Antarctic continent, the sea ice fields also impart a strong influence and therefore may initiate or influence some of the mechanisms discussed. In addition to the mechanistic possibilities, a number of consistent regional links seem to be implied in previous investigations. They repeatedly show considerable ties between the Indian and Pacific Ocean sectors of the Antarctic polar seas and extrapolar regions, but relatively few with the Atlantic. The previous studies suggest that there may be considerable seasonal variability in the nature of the relationships, which will undermine the extent of correlations found here. However, even when considering the full time series for all seasons, we still seem to find concentrations of teleconnections in these same regions. For the Indian Ocean, a region in which the areal extent of the ice cover is small given the equatorward disposition of the Antarctic continent, there are a number of unique interesting features, as noted by Taljaard (1972). For example, this strong sensitivity may be a consequence of the more northern position, which also leads to the closest proximity of the polar and subtropical convergence zones. Perhaps a small change in equatorward ice extent might exert a stronger influence on the westerlies and meridional gradients because of this proximity and northward extension.

6. Conclusions

This paper examines the spatial and temporal variations of Antarctic sea ice and investigates the linear relationships of the sea ice with global climate variability, as defined by general climate indices and global

surface air temperatures. From our analysis we draw the following conclusions.

1) Regarding the nature of the variability documented within the Antarctic sea ice fields, the net trend in the Antarctic sea ice edge is positive over the last 18 yr, shifting on average by $0.011 \pm 0.043°$ of lat equatorward per year [consistent with the recent analyses of Cavalieri et al. (1997) for the last 18 yr of data]. There is considerable variability about this trend, showing an rms noise level of 0.78°, equivalent to approximately 1–4 decades of trend. Furthermore, there is considerable spatial heterogeneity in the trend (Fig. 1), showing significant increase in the Ross and Weddell Seas, and strong retreat in the Amundsen and Bellingshausen Seas of the eastern Pacific [consistent with the recent analysis of Stammerjohn and Smith (1997), among others]. The sea ice edge shows an annual average spatial decorrelation length of approximately 12° longitude.

   The detrended monthly sea ice edge anomaly series, spatially averaged into 12° longitude bands ($\langle$SIE*$\rangle$), contains variance over all frequency bands consistent with a red spectrum, but it does show a significant concentration, above the red spectral background, at periods of ~5 and 1.5–2 yr. The former is most prominent in the western Indian Ocean and central–eastern Pacific Ocean. It shows an eastward propagation of 45° long yr^{-1}, consistent with a complete migration around the Antarctic in approximately 8 yr (though the migration may not be continuous around the continent in the sea ice edge signal). This is consistent with the general phase speed of the ACW described by White and Peterson (1996). The primary complex EOF mode of the SIE* series, representing 46% of the total variance, shows an eastward migration at this same rate. It also shows the strongest variance is concentrated in the Ross Sea and Weddell gyre region (with opposite polarity). Variability in the 1–2-yr band is concentrated in the eastern Ross Sea and Weddell Sea; it does not propagate.
2) The $\langle$SIE*$\rangle$, particularly within wide bands of the Amundsen Sea, Bellingshausen Sea, and Weddell gyre region extended to 40°E, show significant correlations (Fig. 4) with indices representing ENSO variability (Niño-3), Indian Ocean SST, and tropical Pacific precipitation. The strongest correlations are with the Indian Ocean SST ($r = 0.69$). The correlation structure reveals a coherent propagating pattern in which the area of peak correlation migrates to the east at a rate of approximately 45° yr^{-1}. This eastward-migration speed is consistent with the phase propagation speed of the ACW (White and Peterson 1996), and with the phase speed of the SIE* coherent structure mentioned in conclusion 1 above. However, the propagating pattern seems discontinuous in the Indian Ocean sector of the Antarctic, so it may be more representative of subpolar gyre variations. The correlation structure also shows that the relationship between the climate indices and $\langle$SIE*$\rangle$ extends over a full range of lead–lag relationships (e.g., those for which changes in $\langle$SIE*$\rangle$ presage changes in extrapolar climate, and vice versa). However, this highlights the temporal–spatial quasiperiodic nature of the $\langle$SIE*$\rangle$ and temporal quasiperiodic nature of the climate indices, which (among other things) prevents us from being able to identify any particular lag as representative of a direct link between the $\langle$SIE*$\rangle$ and extrapolar climate indices (i.e., we cannot identify the direction of causality). Regardless, the results show a considerable degree of covariability between $\langle$SIE*$\rangle$ and extrapolar climate indices.
3) The $\langle$SIE*$\rangle$ were correlated to detrended globally distributed surface air temperature anomaly time series (SAT*) to reveal the specific nature of any relationships between the Antarctic sea ice fields and extrapolar climate. Four typical teleconnection patterns were found: 1) an ENSO-like pattern in the Tropics with strong correlations in the tropical Indian Ocean and North America, 2) a teleconnection pattern between the eastern Pacific region of the Antarctic and western–central tropical Pacific, 3) an Antarctic dipole across the Drake Passage, and 4) meridional banding structures in the central Pacific and Atlantic extending from polar regions to the Tropics (some even to the Northern Hemisphere).
4) Statistical (bootstrap) tests, designed to take into account temporal and spatial covariability inherent within the series being correlated, reveal that the correlations between $\langle$SIE*$\rangle$ and SAT* yield considerably more (almost twice as many) significant correlations than expected by correlating the SAT* with noise containing the same spectral coloring (including the quasiperiodic components) as the $\langle$SIE*$\rangle$ data. With this quasiperiodic colored noise, we expect significant correlations over ~4% of the global SAT* grid; the actual $\langle$SIE*$\rangle$ data yield 8%.
5) An EOF analyses of the SAT* fields and correlation fields (showing the global distribution of correlation coefficients between $\langle$SIE*$\rangle$ and SAT*) were applied in an attempt to distinguish those regions representing physically meaningful links within the 8% of the global grid producing significant correlations, from those arising by coincidental alignment of noise (expected over 4% of the global grid). The correlation fields capture many of the spatial characteristics displayed in the lowest-order modes of the SAT* fields, with particularly strong links between the sea ice fields in the eastern–central Pacific and Weddell gyre region, with the regions influenced by the ENSO phenomenon (e.g., tropical Pacific, western Pacific, and Indian Ocean). The strongest correlations associated with the ENSO signal appear to occur with the $\langle$SIE*$\rangle$ at 120°–132°W (Amundsen Sea area) lagging the SAT* by 6 months, so that a

boreal fall–winter El Niño event, for example, would have a corresponding signature in ⟨SIE*⟩ 6 months later during early ice growth in the austral fall–winter. This region of the Antarctic also links with a meridional banding structure running the full extent of the North and South Atlantic.

In addition, the EOF decomposition of the correlation fields, concentrating on those maps for which the spatial area of significant correlations (at the 95% confidence level) exceeds that expected in the quasiperiodic colored noise, displays many of the spatial patterns captured in the first few SAT* modes (e.g., ENSO), as well as a number of patterns that seem to reflect the unique nature of the polar–extrapolar relationships. Most notable is a strong Antarctic dipole, between the eastern Pacific and western Weddell, and the Atlantic banding structure mentioned above. There is also a persistent link between the ice at several locations around the Antarctic and the Indian Ocean.

We compare the spatial distribution of significant correlations to the patterns dominating the SAT* EOF modes to see what fraction of significant correlations coincides with these regions. For the cases examined (those of Fig. 6), 50%–70% of the significant area overlaps with the highest-amplitude portions of the modes. This is consistent with an interpretation that significant correlations within regions representing the principal climate patterns, or some fraction of them, are likely to be physically meaningful, while the fraction of significant correlations lying outside of these regions arises from coincidental alignment of noise. This interpretation should eventually be tested against models that have a demonstrated ability for simulating observed global climate teleconnections.

Acknowledgments. The authors thank Drs. Y. Kushnir, D. J. Cavalieri, and S. Jacobs for their helpful discussions and comments. We are especially grateful to Dr. D. J. Cavalieri for providing additional sea ice data. Both SMMR–SSM/I and SSM/I *F13* sea ice concentration data were provided by National Snow and Ice Data Center (NSIDC). Digital data are available from NSIDC distributed Active Archive Center (nsidc@kryos.colorado.edu), University of Colorado at Boulder, Boulder, Colorado. This research was supported in part by Lamont-Doherty Earth Observatory seed money and in part by an environmental research gift from the Ford Motor Company.

APPENDIX

Significance Test for Linear Correlations

a. Local (temporal) significance test

The temporal autocorrelation, or serial correlation, that must be accounted for in the local test (for the correlations in both sections 4a and 4b) implies that the data points within the time series being correlated are not independent. We must thus apply a technique to estimate the number of independent samples in each time series, or the effective degrees of freedom (EDOF). We employ a technique modified from Davis (1976) and used in many subsequent climate studies (Chen 1982; Livezey and Chen 1983; Zhao and Khalil 1993). An estimation of the effective time between independent samples is calculated from the autoregressive properties of both time series being correlated:

$$\tau = \left[1 + 2 \sum_{i=1}^{M<N} C_{SS} C_{II}\right] \Delta t, \tag{A1}$$

where Δt is the sampling interval, N is the sample length, M is the number of lags used in estimating τ, and the C's are the autocorrelations at lags Δt for the Antarctic ⟨SIE*⟩ (S) and climate series (I). We use the biased form of the autocorrelation function for C's to reduce sampling errors at large lags and choose $M = 60$ months. In other words, we account for the effect of autocorrelation over 5-yr windows, which is adequate for this study since we are predominantly focusing on the interannual variabilities with periods of ~5 yr or less (the time series are too short to meaningfully evaluate the significance of longer-period variance).

Based on τ, the number of independent samples, or EDOF, is given as

$$\text{EDOF} = \frac{N\Delta t}{\tau}. \tag{A2}$$

Once the EDOF is determined, local significance levels are determined in the standard way using EDOF as the number of independent samples in the correlations. These local confidence levels of the various correlations, at each grid point, are presented in each of the correlation maps, Figs. 4 and 6.

b. Field (spatial) significance test

A similar, though more difficult, problem involves the spatial autocorrelation of the global surface air temperature anomaly (SAT*) data that must be accounted for with the field significance test. As previously stated, the spatial decorrelation length of ⟨SIE*⟩ is about 12° long. When the SIE* are averaged into 12° long bands, we produce averaged ⟨SIE*⟩ that are approximately independent in space. Therefore, the local significance test is adequate for the results of Fig. 4, and a field test is not necessary. However, large-scale coherent patterns, such as that associated with ENSO, the PNA pattern, etc., exist in the global SAT* data. Therefore, correlations involving the SAT* fields demand that a field significant test must be considered to evaluate the contribution of the inherent spatial autocorrelation. In order to properly account for the natural spectral coloring of

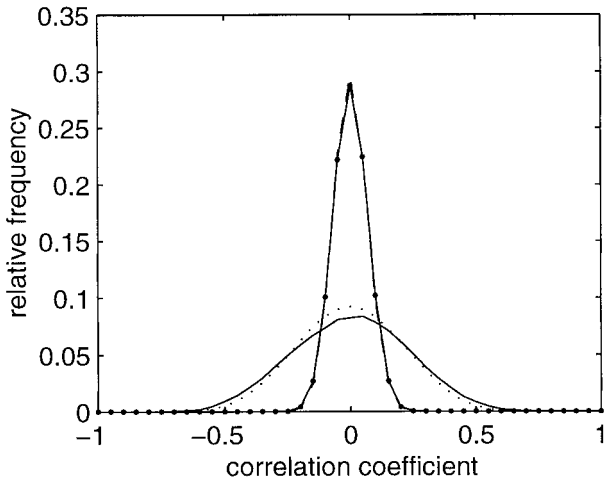

FIG. A1. Distributions of correlations between the global temperature anomalies and the ⟨SIE*⟩ in three climate-sensitive areas with leads 6 months to lags 2 yr (solid line), 1000 white noise series (dot-dashed line), 1000 randomly shuffled ⟨SIE*⟩ series (dashed line), and 1000 colored noise series (dotted line). Note that the white noise distribution overlaps with the shuffled series distribution.

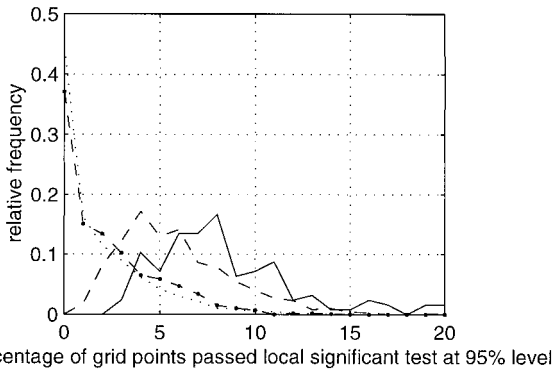

FIG. A2. The percentage of total grid points in each correlation map that passed the local significance test at 95% confidence level for ⟨SIE*⟩ in the three climate-sensitive regions with ⟨SIE*⟩ leading 2 yr to lagging 2 yr (solid line), and for white noise (dot-dashed line), randomly shuffled series (dotted line), and colored noise (dashed line).

the data, we employ a bootstrap method to evaluate this field significance.

The method involves the following. First, a discrete Fourier transform is applied to an ⟨SIE*⟩ series. The phase of this transform for the positive frequencies is replaced by evenly distributed white noise scaled between $\pm\pi$, while the amplitude of the transform is unaltered. The phase for the negative frequencies was generated from the white noise of the positive frequencies so as to preserve the spectral symmetry of a real series. The inverse Fourier transform of this modified series creates a colored noise series that retains the ''redness'' (or internal temporal memory) of the original time series, as well as any inherent periodicities above the general red noise.

This procedure is repeated 1000 times with 1000 sets of different random phases for each ⟨SIE*⟩ series. We also generate 1000 normally distributed white noise ⟨SIE*⟩ series and 1000 randomly ''shuffled'' ⟨SIE*⟩ series. The former disallows any dependency between neighboring data points in the time series (i.e., zero autocorrelation). This is physically incorrect but will provide a significance test consistent with the use of standard statistical tables that assume all data points are independent. The shuffled noise preserves the amplitudes of the original ⟨SIE*⟩ series but not the original autocorrelation. Instead it introduces random spectral coloring (i.e., random autocorrelation).

The global SAT* are correlated with these three groups of simulated random noise. Distributions of the results are presented in Fig. A1 and compared with the distribution of the correlations obtained using real ⟨SIE*⟩ series. In the field test, the real ⟨SIE*⟩ series only include the three climatically sensitive regions: 1°–48°E, 156°–48°W, and 36°–12°W (i.e., those regions producing the strongest correlations with global SAT* and thus in most need of statistical assessment). For the real data correlation distribution, we also include results for correlations with ⟨SIE*⟩ from leading 2 yr to lagging 2 yr, at 6-month intervals.

The most obvious result emerging from comparison of the distributions is that the influence of serial correlation in the ⟨SIE*⟩ data cannot be neglected in the confidence tests (i.e., assumption of white noise or independent samples grossly distorts the statistical significance test, allowing significance at considerably lower r values than should be admitted). Results from the randomly shuffled series are very close to the white noise results, while correlations with colored noise series are significantly closer to the observed population as expected since they most closely preserve potential noise characteristics of the data. However, even though the colored noise distribution is similar to the observed distribution, the large sample size assures that the two distributions are significantly different (at 99.5% confidence level using a chi-square similarity test). That is, there are more high correlations in the data than expected from correlations with random series of the same general spectral coloring (including the inherent quasiperiodic nature).

The field test is now applied as follows. For each correlation map, the fraction of total grid points that exceeded the 95% confidence level in the local significance test is determined. A similar fraction was computed for each of the 1000 colored noise series, 1000 shuffled series, and 1000 white noise series experiments (in which the noise was correlated to the SAT* in the same manner in which the ⟨SIE*⟩ were correlated). Distributions of fractions for each of these experiments are then compared to that for the data to determine if the data contain more significant correlations around the globe than expected from correlations with random noise of different color (Fig. A2). These distributions,

TABLE A1. Field confidence levels of the four correlation maps in Fig. 6 using the colored noise distribution. The results are even more significant for those less realistic noise distributions (white and shuffled noise).

SIE	Ice lag	Field confidence level
0°–12°E	0	92%
72°–84°W	0	89%
120°–132°W	0	78%
120°–132°W	6 months	98%

including those with noise, reflect the influence of the spatial coherence existing in the surface temperature field.

As seen in Fig. A2, the distribution of significant correlations from the real ⟨SIE*⟩ series, relative to that for the various noise series, is shifted to higher percentages, reflecting a higher fraction of significant correlations. The mode of significant correlations (i.e., the center of the primary mode of the distributions in Fig. A2) is 8% for the data and 4% from the colored noise series. The means are 8.4% and 5.8%, for the data and colored noise, respectively. To evaluate the significance of this difference in mean values, we randomly selected 126 numbers (the sample size of the data) from 1000 colored noise results used to generate the colored noise distribution, and then calculated the mean of these 126 numbers. This process was repeated 10 000 times. The 10 000 means have a Gaussian distribution centered at 5.8% with a standard deviation of 0.26% (precisely the value predicted by the central limit theorem). The data mean lies over 9 standard deviations from the mean of the colored noise. Therefore, the data show significantly more correlations than expected from correlating to random noise.

Furthermore, the shift in distributions between the real and colored noise distributions indicates that there are more significant correlations in the data than in the colored noise series in the fraction range more than 6% (i.e., there are more significant correlations covering more than 6% of the global grid than expected by random chance, even accounting for the spectral coloring of the data). A chi-square test of similarity suggests that the distributions for the data and colored noise (that distribution most representative of the data) are different at the 99.5% confidence level.

The distribution of the noise can now be used to evaluate the significance of the individual correlation maps presented in Fig. 6 (the previous test result was for the collective total of all maps). The field confidence levels of the four correlation maps presented in Fig. 6 are given in Table A1. For those bands in which the significance is lower than 95%, the implication is that the spatial correlation pattern is dominated by spatially coherent patterns in the SAT* so that geographically independent significant correlations are sparse in those maps. Clearly, the different field confidence levels in these four maps imply that the ⟨SIE*⟩ at different regions respond to different characteristics of the global signal.

REFERENCES

Bromwich, D. H., B. Chen, and K. M. Hines, 1998: Global atmospheric impacts induced by year-around open water adjacent to Antarctica. *J. Geophys. Res.*, **103** (D10), 11 173–11 189.

Cane, M. A., S. E. Zebiak, and S. C. Dolan, 1986: Experimental forecasts of El Nino. *Nature*, **322,** 827–832.

Carleton, A. M, 1988: Sea ice–atmosphere signal of the Southern Oscillation in the Weddell Sea, Antarctica. *J. Climate*, **1,** 379–388.

——, 1989: Antarctic sea-ice relationships with indices of the atmospheric circulation of the Southern Hemisphere. *Climate Dyn.*, **3,** 207–220.

Cavalieri, D. J., P. Gloersen, C. L. Parkinson, J. C. Comiso, and H. J. Zwally, 1997: Observed hemispheric asymmetry in global sea ice changes. *Science*, **278,** 1104–1106.

Charles, C. D., D. E. Hunter, and R. G. Fairbanks, 1997: Modulating influence of the monsoon and the Southern Oscillation in a 150 year long coral record of tropical Indian Ocean surface temperature. *Science*, **277,** 925–928.

Chen, W. Y., 1982: Fluctuations in Northern Hemisphere 700-mb height field associated with the Southern Oscillation. *Mon. Wea. Rev.*, **110,** 808–823.

Chiu, L. S., 1983: Antarctic sea ice variations 1973–1980. *Variations in the Global Water Budget*, A. Street-Perrott, M. Beran, and R. Ratcliffe, Eds., Reidel, 301–311.

Comiso, J. C., D. J. Cavalieri, C. L. Parkinson, and P. Gloersen, 1997: Passive microwave algorithms for sea ice concentration: A comparison of two techniques. *Remote Sens. Environ.*, **60** (3), 357–384.

Dai, A., I. Y. Fung, and A. D. Del Genio, 1997: Surface observed global land precipitation variations during 1900–1988. *J. Climate*, **10,** 2943–2962.

Davis, R. E., 1976: Predictability of sea surface temperature and sea level pressure anomalies over the North Pacific Ocean. *J. Phys. Oceanog.*, **6,** 249–266.

Fletcher, J. O., 1969: Ice extent in the southern oceans and its relation to world climate. *J. Glaciol.*, **15,** 417–427.

Gloersen, P., 1995: Modulation of hemispheric sea-ice cover by ENSO events. *Nature*, **373,** 503–506.

——, and W. J. Campbell, 1991: Recent variations in Arctic and Antarctic sea-ice covers. *Nature*, **352,** 33–36.

——, ——, D. J. Cavalieri, J. C. Comiso, C. L. Parkinson, and H. J. Zwally, 1992: Arctic and Antarctic sea ice, 1978–1987: Satellite passive microwave observations and analysis. NASA SP-511, 290 pp.

Godfred-Spenning, C. R., and I. Simmonds, 1996: An analysis of Antarctic sea ice and extratropical cyclone associations. *Int. J. Climatol.*, **16,** 1315–1332.

Grumbine, R. W., 1994: A sea-ice albedo experiment with the NMC Medium Range Forecast model. *Wea. Forecasting*, **9,** 453–456.

Hansen, J. E., and S. Lebedeff, 1987: Global trends of measured surface air temperature. *J. Geophys. Res.*, **92,** 13 345–13 372.

——, G. Russell, D. Rind, P. Stone, A. Lacis, S. Lebedeff, R. Rudey, and L. Travis, 1983: Efficient three-dimensional global models for climate studies: Models I and II. *Mon. Wea. Rev.*, **111,** 609–662.

Hines, K. M., and D. H. Bromwich, 1999: The roles of Arctic and Antarctic sea ice in forcing global climate. Preprints, *Fifth Conf. on Polar Meteorology and Oceanography*, Dallas, TX, Amer. Meteor. Soc., 39–43.

Horel, J. D., 1984: Complex principal component analysis: Theory and examples. *J. Climate Appl. Meteor.*, **23,** 1660–1673.

Hurrell, J. W., 1995: Decadal trends in the North Atlantic Oscillation: Regional temperature and precipitation. *Science*, **269,** 677–679.

Jacobs, S. S., and J. C. Comiso, 1997: Climate variability in the Amundsen and Bellingshausen Seas. *J. Climate,* **10,** 697–709.
James, I. N., 1988: On the forcing of planetary-scale Rossby waves by Antarctica. *Quart. J. Roy. Meteor. Soc.,* **114,** 619–637.
Johannessen, O. M., M. Miles, and E. Bjorgo, 1995: The Arctic's shrinking sea ice. *Nature,* **376,** 126–127.
Jones, P. D., 1994: Hemispheric surface air temperature variations: A reanalysis and an update to 1993. *J. Climate,* **7,** 1794–1802.
Julian, P. R., and R. M. Chervin, 1978: A study of the Southern Oscillation and Walker circulation phenomenon. *Mon. Wea. Rev.,* **106,** 1433–1451.
Kalnay, E., and Coauthors, 1996: The NCEP/NCAR 40-Year Reanalysis Project. *Bull. Amer. Meteor. Soc.,* **77,** 437–471.
Karoly, D. J, 1989: Southern Hemisphere circulation features associated with El Niño–Southern Oscillation events. *J. Climate,* **2,** 1239–1252.
Katz, R. W., and B. G. Brown, 1991: The problem of multiplicity in research on teleconnections. *Int. J. Climatol.,* **11,** 505–513.
Kawamura, R., 1994: A rotated EOF analysis of global sea surface temperature variability with interannual and interdecadal scales. *J. Phys. Oceanogr.,* **24,** 707–715.
Krishnamurti, T. N., S.-H. Chu, and W. Iglesias, 1986: On the sea level pressure of the Southern Oscillation. *Arch. Meteor., Geophys. Bioklimatol.,* **34A,** 385–425.
Kumar, K. K., 1997: Seasonal forecasting of Indian summer monsoon rainfall: Diagnostics and synthesis of regional and global signals. Ph.D. thesis, Indian Institute of Tropical Meteorology, 301 pp. [Available from Indian Institute of Tropical Meteorology, Pashan Rd., Pune 411 008, India.]
Large, W. G., and H. van Loon, 1989: Large-scale, low-frequency variability of the 1979 FGGE surface buoy drifts and winds over the Southern Hemisphere. *J. Phys. Oceanogr.,* **19,** 216–232.
Ledley, T. S., and Z. Huang, 1997: A possible ENSO signal in the Ross Sea. *Geophys. Res. Lett.,* **24,** 3253–3256.
Livezey, R. E., and W. Y. Chen, 1983: Statistical field significance and its determination by Monte Carlo techniques. *Mon. Wea. Rev.,* **111,** 46–59.
Meehl, G. A., 1984: Modeling the earth's climate. *Climatic Change,* **6,** 259–286.
——, 1988: Tropical–midlatitude interactions in the Indian and Pacific sectors of the Southern Hemisphere. *Mon. Wea. Rev.,* **116,** 472–484.
——, 1990: Seasonal cycle forcing of El Nino–Southern Oscillation in a global, coupled ocean–atmosphere GCM. *J. Climate,* **3,** 72–98.
——, 1991: A reexamination of the mechanism of the semiannual oscillation in the Southern Hemisphere. *J. Climate,* **4,** 911–926.
——, and W. M. Washington, 1990: CO_2 climate sensitivity and snow–sea-ice albedo parameterization in an atmospheric GCM coupled to a mixed layer ocean model. *Climatic Change,* **16,** 283–306.
Mitchell, J. F. B., and T. S. Hills, 1986: Sea-ice and the Antarctic winter circulation: A numerical experiment. *Quart. J. Roy. Meteor. Soc.,* **112,** 953–969.
Mo, K. C., and G. H. White, 1985: Teleconnections in the Southern Hemisphere. *Mon. Wea. Rev.,* **113,** 22–37.
National Snow and Ice Data Center, 1997: Passive microwave derived daily polar sea ice concentration time series. Digital data. [Available from NSIDC Distributed Active Archive Center, University of Colorado at Boulder, Boulder, CO 80309; also available from nsidc@kryos.colorado.edu.]
Orlanski, I., J. Katzfey, C. Menendez, and M. Marino, 1991: Simulation of an extratropical cyclone in the Southern Hemisphere: Model sensitivity. *J. Atmos. Sci.,* **48,** 2293–2311.
Parish, T. R., 1984: A numerical study of strong katabatic winds over Antarctica. *Mon. Wea. Rev.,* **112,** 545–554.
——, 1992: On the role of Antarctic katabatic winds in forcing large-scale tropospheric motions. *J. Atmos. Sci.,* **49,** 1374–1385.
Parker, D. E., P. D. Jones, A. Bevan, and C. K. Folland, 1994: Interdecadal changes of surface temperature since the late 19th century. *J. Geophys. Res.,* **99,** 14 373–14 399.
——, C. K. Folland, and M. Jackson, 1995: Marine surface temperature: Observed variations and data requirements. *Climatic Change,* **31,** 559–600.
Parkinson, C. L., 1992: Interannual variability of monthly southern ocean sea ice distributions. *J. Geophys. Res,* **97,** 5349–5363.
——, 1994: Spatial patterns in the length of the sea ice season in the Southern Ocean, 1979–1986. *J. Geophys. Res.,* **99,** 16 327–16 339.
Peng, G. B., and P. K. Wang, 1989: Influence of the Antarctic sea-ice on the Northwest Pacific sub-tropical high and its background of ocean–atmospheric circulation. *Chin. Sci. Bull.,* **34,** 1463–1465.
Peterson, R. G., and W. B. White, 1998: Slow teleconnections linking the Antarctic Circumpolar Wave with the tropical El Niño–Southern Oscillation. *J. Geophys. Res.,* **103** (C11), 24 573–24 583.
Rasmusson, E. M., and T. H. Carpenter, 1982: Variations in tropical sea surface temperature and wind fields associated with the Southern Oscillation/El Nino. *Mon. Wea. Rev.,* **110,** 354–384.
Reuter, E., 1936: Die synoptische Darstellung der 1/2 jahrigen Druckwelle. *Veröff. Geophys. Inst. Univ. Leipzig,* **7,** 257–295.
Reynolds, R. W., and T. M. Smith, 1994: Global sea surface temperature analysis. *J. Climate,* **7,** 929–948.
Rind, D., R. Healy, C. Parkinson, and D. Martinson, 1995: The role of sea ice in $2XCO_2$ climate model sensitivity. Part I: The total influence of sea ice thickness and extent. *J. Climate,* **8,** 449–463.
Roberts, J., and T. D. Roberts, 1978: Use of the Butterworth low-pass filter for oceanographic data. *J. Geophys. Res.,* **83,** 5510–5514.
Schwerdtfeger, W., 1960: The seasonal variation of the strength of the southern circumpolar vortex. *Mon. Wea. Rev.,* **88,** 203–208.
——, 1962: The southern circumpolar vortex and the spring warming of the polar stratosphere. *Meteor. Abh.,* **36,** 207–224.
——, and St. J. Kachelhoffer, 1973: The frequency of cyclone vortices over the southern ocean in relation to the extension of the pack ice belt. *Antarct. J.,* **8,** 234.
Simmonds, I., and M. Dix, 1986: The circulation changes induced by the removal of Antarctic sea ice in a July general circulation model. *Extended Abstracts, Second Int. Conf. on Southern Hemisphere Meteorology,* Wellington, New Zealand, Amer. Meteor. Soc., 107–110.
——, and X. Wu, 1993: Cyclone behaviour response to changes in winter Southern Hemisphere sea-ice concentration. *Quart. J. Roy. Meteor. Soc.,* **119,** 1121–1148.
——, and T. H. Jacka, 1995: Relationships between the interannual variability of Antarctic sea ice and the Southern Oscillation. *J. Climate,* **8,** 637–647.
——, and R. Law, 1995: Associations between antarctic katabatic flow and the upper level winter vortex. *Int. J. Climatol.,* **15,** 403–421.
——, and D. A. Jones, 1998: The mean structure and temporal variability of the semiannual oscillation in the southern extratropics. *Int. J. Climatol.,* **18,** 473–504.
Smith, R. C., S. E. Stammerjohn, and K. S. Baker, 1996: Surface air temperature variations in the western Antarctic Peninsula region. *Foundations for Ecological Research West of the Arctic Peninsula,* R. M. Ross, E. E. Hofmann, and L. B. Quetin, Eds., Antarctic Research Series, Vol. 70, Amer. Geophys. Union, 105–121.
Smith, S. R., and C. R. Stearns, 1993: Antarctic pressure and temperature anomalies surrounding the minimum in the Southern Oscillation index. *J. Geophys. Res.,* **98** 13 071–13 083.
Stammerjohn, S. E., and R. C. Smith, 1996: Spatial and temporal variability of the western Antarctic Peninsula sea ice coverage. *Foundations for Ecological Research West of the Antarctic Peninsula,* R. M. Ross, E. E. Hofmann, and L. B. Quetin, Eds.,

Antarctic Research Series, Vol. 70, Amer. Geophys. Union, 81–104.

——, and ——, 1997: Opposing Southern Ocean climate patterns as revealed by trends in regional sea ice coverage. *Climatic Change,* **37,** 617–639.

Streten, N. A., and D. J. Pike, 1980: Characteristics of the broadscale Antarctic sea ice extent and the associated atmospheric circulation 1972–1977. *Arch. Meteor., Geophys. Bioklimatol.,* **29A,** 279–299.

Taljaard, J. J., 1972: Physical features of the Southern Hemisphere. *Meteorology of the Southern Hemisphere, Meteor. Monogr.,* No. 35, Amer. Meteor. Soc., 1–8.

Thompson, D. W. J., and J. M. Wallace, 1998: The Arctic Oscillation signature in the wintertime geopotential height and temperature fields. *Geophys. Res. Lett.,* **25,** 1297–1300.

Tourre, M. Y., and W. B. White, 1995: ENSO signals in global upper-ocean temperature. *J. Phys. Oceanogr.,* **25,** 1317–1332.

Trenberth, K. E., 1980: Planetary waves at 500 mb in the Southern Hemisphere. *Mon. Wea. Rev.,* **108,** 1378–1389.

——, W. G. Large, and J. G. Olson, 1990: The mean annual cycle in global ocean wind stress. *J. Phys. Oceanogr.,* **20,** 1742–1760.

van Loon, H., 1967: The half-yearly oscillations in middle and high southern latitudes and the coreless winter. *J. Atmos. Sci.,* **24,** 472–486.

——, 1972: Wind in the Southern Hemisphere. *Meteorology of the Southern Hemisphere, Meteor. Monogr.,* No. 35, Amer. Meteor. Soc., 87–100.

——, 1984: The Southern Oscillation. Part III: Associations with the trades and with the trough in the westerlies of the South Pacific Ocean. *Mon. Wea. Rev.,* **112,** 947–954.

——, and R. L. Jenne, 1972: The zonal harmonic standing waves in the Southern Hemisphere. *J. Geophys. Res.,* **77,** 992–1003.

——, ——, and K. Labitzke, 1973: Zonal harmonic standing waves. *J. Geophys. Res.,* **78,** 4463–4471.

Walker, G. T., 1923: Correlation in seasonal variations of weather, VIII. *Mem. Indian Meteor. Dept.,* **24,** 75–131.

——, 1924: Correlation in seasonal variations of weather, IX. *Mem. Indian Meteor. Dept.,* **24,** 275–322.

Wallace, J. M., and R. E. Dickinson, 1972: Empirical orthogonal representation of time series in the frequency domain. Part I: Theoretical considerations. *J. Appl. Meteor.,* **11,** 887–900.

Walsh, J. E., 1983: The role of sea ice in climatic variability: Theories and evidence. *Atmos.–Ocean,* **21** (3), 229–242.

Weatherly, J. W., J. E. Walsh, and H. J. Zwally, 1991: Antarctic sea ice variations and seasonal air temperature relationships. *J. Geophys. Res.,* **96,** 15 119–15 130.

White, W. B., and R. G. Peterson, 1996: An Antarctic circumpolar wave in surface pressure, wind, temperature and sea ice extent. *Nature,* **380,** 699–702.

——, S.-C. Chen, and R. G. Peterson, 1998: The Antarctic circumpolar wave: A beta effect in ocean–atmosphere coupling over the Southern Ocean. *J. Phys. Oceanogr.,* **28,** 2345–2361.

Yuan, X., M. A. Cane, and D. G. Martinson, 1996: Climate variation—Cycling around the South Pole. *Nature,* **380,** 673–674.

Zhao, W., and M. A. K. Khalil, 1993: The relationship between precipitation and temperature over the contiguous United States. *J. Climate,* **6,** 1232–1236.

Zwally, H. J., J. C. Comiso, C. L. Parkinson, W. J. Campbell, F. D. Carsey, and P. Gloerson, 1983: Antarctic sea ice, 1973–1976: Satellite passive-microwave observations. NASA SP-459, 200 pp.